PLANT MICROTECHNIQUE WITH RESIN - TOWARDS PLANT HISTOLOMICS

Ivan T. Cerritos-Castro, Araceli Patrón-Soberano, Ana P. Barba de la Rosa*.

IPICYT, Instituto Potosino de Investigación Científica y Tecnológica A.C., San Luis Potosí, México.

*For correspondence: apbarba@ipicyt.edu.mx
Tel: 52 (444) 8342000 Ext. 2082

ABSTRACT

Plant microtechnique; a laborious discipline that provides little data. The difficulty in handling paraffin sections and the lack of a strategy for analyzing micrographs discourage its use. Nevertheless, it provides the fundamental cellular context for understanding the function of biomolecules. In this work, we standardized a resin embedding method, a chemical treatment for slides, a trichrome staining, and an immunostaining. We also developed a strategy for micrograph segmentation, morphometric and compositional analysis, and proposed the basis for a histolomic field. The resin-based microtechnique was easier than the paraffin-based ones, revealed a wealth of morphological and compositional information, and was reproducible in a variety of tissues of plant species. Histolomics allowed numerical comparisons of primary morphometric and compositional features such as size or protein content, as well as composite features such as the C_4 kranz anatomy. This method takes the cellular context to the field of omics.

INTRODUCTION

Tissues are the result of the interaction of millions of ordered molecules. Our understanding of their nature and function is largely based on their molecular disassembling for *in vitro* studies. This approach has been strengthened by omics, which correlate *in vitro* molecular abundances with the phenotype of tissues, organs and even whole organisms[1]. However, the abundance of a molecule is just as important as its location, as it is related to its function and defines the composition and morphology of tissues[2,3].

Plant histology describes the morphology and composition of tissues and cells[4]. Along with immunostaining, it localizes the abundance of molecules in tissues[3]. Despite its importance, plant histology is underutilized in plant research. The main reasons may be the dexterity required by their methods (microtechnique), and the lack of a harmonized strategy for analyzing their results. Compared to *in vitro* methods, plant microtechnique is more artisanal[5]. Classic microtechnique consist of sample fixation, dehydration, paraffin embedding, sectioning, affixing (attachment to glass slides), staining, immunostaining, dehydration, mounting (resin and coverslip placement), and microscopy[6]. Each step is susceptible to failure, but especially from affixing to mounting, which we call the dexterity-dependent steps. Paraffin sections are fragile; they may be wrinkled or broken during affixing and may become detached or scratched during subsequent steps. In addition, paraffin is removed from the section after the affixing step, making the tissue even more susceptible to damage.

If we replace the paraffin with a permanent and more stable support, the dexterity-dependent steps will be easier. LR White resin, an acrylic resin, is an embedding medium used primarily in Transmission Electron Microscopy (TEM), but is compatible with light microscopy[5]. Unlike paraffin, its hydrophilic nature allows analysis on sections without removing the resin. That provides mechanical support to the section during dexterity-dependent steps, reducing section breakage and scratches. On the other hand, effective glass slide cleaning can prevent section wrinkles, and effective "gluing" can

prevent section detachment. Various acidic and oxidizing solutions have been formulated to clean and, at the same time, “activate” the slides[7–9]. Activation creates hydroxyl groups that increase the wettability of the glass surface. The hydroxyl groups can then react with (3-aminopropyl)triethoxysilane (AES) in a "gluing" process to increase the adhesiveness of the slide[10].

Once the section is affixed, staining and immunostaining are the basic methods of plant microtechnique to study the morphology, general composition, and specific location of proteins in a tissue.[6] Johansen's staining has been the classic method for plant paraffin sections since 1940 and has been modified several times[6,11–14]. It is based on safranin, which stains mainly cell wall lignin and suberin in magenta, and fast green, which stains mainly cytoplasmic proteins in turquoise[15–17]. Johansen's staining gives a picture of the general composition of the whole tissue, while immunostaining gives a picture of the abundance of specific proteins at specific locations in the tissue[3,6]. In contrast, resin sections are usually stained only with toluidine blue for light microscopy, which stains the entire tissue blue[18].

After a successful microtechnique, scientists often don't know what to do with the micrographs and are limited to pointing out tissue abnormalities or the location of immunolabel. If we define and systematize a histological analysis, scientists will be able to exploit the information from a micrograph. The primary features of a tissue are described in terms of morphology, morphometry and composition. Morphology qualitatively describes the overall shape of a plant, organ, or tissue; morphometry quantitatively describes the number, size and shape of an element; and composition describes the overall molecular abundance in cell structures[4,19,20]. Tissue staining allows for boundary-based morphological and morphometric analysis, as well as color-based compositional analysis, which is typically performed manually and with the naked eye. However, color measurement and image segmentation are digital tools that can provide comprehensive numerical descriptions of a tissue that go beyond the naked eye[21]. On the whole, an easier and standardized microtechnique along with a harmonized and comprehensive digital analysis of micrographs would take us from histology to the "histolomics" research.

Here, we present a resin-based plant microtechnique to facilitate the dexterity-dependent steps, and propose a strategy for analyzing micrographs: the histolomics. We standardised a method for resin embedding, tested several solutions for cleaning, activating, and gluing of glass slides, developed a trichrome staining for resin sections, and combined it with immunostaining. We then applied on amaranth and several C_3 and C_4 plant leaves commonly used in plant research. C_4 plants have an evolved leaf morphology called "Kranz anatomy" that enhances carbon fixation that C_3 plants lack, providing a framework to study[22]. Finally, we defined and measured morphometric and compositional features to quantitatively characterize and compare the tissues.

RESULTS

Glass slides activation and gluing

We tested several solutions for cleaning and activating glass slides. Sulphocromic and Piranha solutions gave the best results: the highest wettability and correspondingly the lowest contact angle. We then "glued" the activated slides with AES. All slides showed a decrease in wettability and an increase in contact angle (Fig 1a, c). Finally, a resin section was affixed in each slide and subjected to strong washes. Again, sulphocromic and piranha activated slides gave the best results, retaining the entire section, while others detached fragments or the entire section (Fig. 1 b).

Staining of resin sections

Classic Johansen's staining did not work on resin sections; we reinvented it and made it trichrome. We tested toluidine blue, Johansen's, and Coomassie's staining methods and measured the color acquired by the cell walls (CW), protoplasm (PR) and resin background in the HSB color space (Hue, Saturation and Brightness). For more details on tissue and cell morphology, see Supplementary Fig. 1 and 2. Hue values depended on the dye, and saturation values on the staining performance. In contrast, brightness values depended mainly on the microscope and camera exposure settings and

117 were very similar for all micrographs. Toluidine blue tended to be monochromatic (similar
118 hue values), and Johansen's staining polychromatic (different hue values) but uneven and
119 poorly saturated (Fig. 2). Achieving different hue values between cell structures is
120 important for their identification and micrograph segmentation. The same is true for the
121 saturation between all the tissue and the unstained resin background. By testing
122 combinations, we found that Coomassie's solvent allows staining of resin sections with
123 Coomassie's dye itself and Johansen's dyes (Safranin and Fast Green), producing
124 polychromatic, uniform, and well-saturated colors (Fig 2). We therefore reformulated the
125 Johnanse's staining and added a third dye: Lugol's iodine, creating a trichrome staining
126 (Fig. 3).

127 Trichrome staining revealed the morphology and general composition of amaranth
128 leaf (Supplementary Fig. 3). Individually, fast green stained mainly the protoplasm
129 turquoise, safranin stained most of the tissue magenta, and iodine stained only the starch
130 granules mauve. None stained vacuoles and resin background, and fast green and safranin
131 did not stain starch granules. The protoplasm (PR) encompasses the cytosol and all
132 organelles, including the vacuole. For an accurate description, we coined the term
133 "proteoplasm (PT)" to refer only to the turquoise (proteinaceous) structures of the
134 protoplasm: cytosol and all organelles except the vacuole and starch granules. A
135 differentiating and synergistic effect was observed in the trichrome combination: safranin
136 now selectively stained cell walls, and hue and saturation values increased. The hue
137 change (veering) in the proteoplasm shifted the color from turquoise to blue hues.
138 Differently, the veering in the cell wall divided the color into magenta and reddish hues
139 (Supplementary Fig. 3). We measured the color of cell walls and proteoplasm separately
140 in the epidermis, mesophyll, and bundle sheath. Proteoplasm had similar hues in all
141 tissues. However, the bundle sheath cell wall had magenta, reddish, and even orange
142 hues, while the epidermis and mesophyll cell walls had only magenta hues. In addition,
143 the bundle sheath showed stained and unstained starch granules. This pattern was
144 confirmed by TEM microscopy, which showed electrodense and electrolucent starch
145 granules (Fig. 4).

146 The order and timing of each dye in trichrome staining were important for the
147 color selectivity. A section stained with fast green could be correctly counterstained with
148 safranin for 5 to 10 s, after which safranin replaced fast green (Supplementary Fig. 4). A
149 section stained with safranin could not be correctly counterstained with fast green
150 (Supplementary Fig. 5). Finally, iodine staining (alone or in a counterstain) produced
151 random intensities independent of time: null, intermediate or intense, even between
152 different sections of the same sample on the same slide; we could not identify the reason.
153 However, along the same section, the random intensity obtained was always uniform
154 (Supplementary Fig. 6).
155 For a successful staining and micrograph interpretation, there were some technical
156 issues that need to be taken into account. The orange hue of the bundle sheath cell wall
157 was best observed with the 40X objective and a diaphragm aperture equivalent to the 10X
158 objective. Mounting with entellan improves the sharpness from the start and as it dries.
159 On the other hand, the iodine staining of the starch granules may fade over time, from
160 days to months. For that reason, we recommend that micrographs be taken one to three
161 days after mounting. Finally, it is important to be aware of common artifacts in resin
162 sections for proper histological interpretation (Supplementary Fig. 7).
163
164 ***Resin-based microtechnique resolution***
165 The resin-based microtechnique allowed light microscopy to resolve small
166 organelles and even ultrastructures that would normally require TEM microscopy to
167 observe. Trichrome staining identified the cell wall in magenta to orange, the proteoplasm
168 in turquoise, and the starch granules in mauve. In fact, the proteoplasm showed different
169 saturation values, allowing the identification of the cytosol, chloroplasts, mitochondria,
170 nucleus, and nucleolus, if present (Fig. 5 and Supplementary Fig. 8 and 9). Furthermore, an
171 intensely iodine counterstained paradermal section showed two layers in the epidermal
172 cell wall: an internal orange and an external magenta. This section also showed
173 ultrastructural details of what appeared to be: membranes within vacuoles, chloroplasts

174 with protein granules, unknown rod-shaped organelles, and vesicles transporting cell wall
175 material, among others (Supplementary Fig. 10).
176
177 ***Histolomic analysis***
178 The resin-based microtechnique required a strategy for the analysis of results and
179 towards histolomics research we proposed a pipeline of four steps: visual analysis, color
180 analysis, micrograph segmentation, and data analysis. First, visual analysis consisted of
181 classical qualitative identification of tissues and overall morphology (Supplementary Fig. 1
182 and 2). We also added the identification of organelles and other relevant features visible
183 thanks to the high resolution of resin-based microtechnique. Cross sections of a young and
184 a senescent amaranth leaf were compared. When looking at the entire micrograph,
185 general differences were observed in the senescent leaf such as decreased proteoplasm,
186 increased starch granules, and rounding of the palisade mesophyll. When looking at the
187 enlarged micrograph, small size differences, such as reduction of cell wall thickness,
188 appearance of starch granules in the palisade mesophyll, disappearance of cytosol, and
189 others, were observed in the senescent leaf (Supplementary Fig. 11).
190 Second, the color analysis consisted of measuring the color of the cell structures
191 and assigning them a hue range for color segmentation (Fig. 4). Third, segmentation of the
192 micrographs consisted of digitally isolating cell structures from the background into layers
193 for further data analysis (Supplementary Video 1). The color contrast provided by the
194 trichrome staining allowed to digitally segmenting tissues based on color (composition)
195 and cell boundaries. We semi-automatically segmented cell walls, proteoplasm, and
196 unstained elements (vacuoles, starch granules, and background) based on their hue and
197 saturation differences. The proteoplasm could be further segmented into low-saturated
198 elements (nucleus and cytosol) and high-saturated elements (the rest of the organelles).
199 The layers show tissue composition and localization more clearly than the original
200 micrograph. However, the thin cell walls of the mesophyll lacked continuity, making
201 boundaries-based morphometric analysis impossible (Supplementary Fig. 12). Therefore,
202 we manually segmented the micrograph cell by cell. The previous cross-sections of a

203 young and senescent amaranth leaf were segmented for data analysis (Supplementary Fig.
204 13 and 14).

205 Fourth, data analysis consisted of defining and measuring primary and derived
206 morphometric and compositional features on the layers and comparing them.
207 Morphometric features involved the quantitative measurement of physical traits such as:
208 number, size, perimeter, area, thickness, and circularity. Compositional features involved
209 the semi-quantitative measurement of stained molecules by densitometry (as an SDS-
210 PAGE gel): proteins, lignin and suberin, starch granules, and immunolabels. Smaller and
211 more rounded palisade mesophyll cells, lower cell wall thickness, lower proteoplasm
212 content and significantly higher starch granule content were found in the senescent leaf.
213 On the other hand, the protein content showed a decrease and the lignin content showed
214 no differences (Supplementary Fig. 15).

215 After all, the more colors, the more information to analyze. Intense iodine
216 counterstaining allowed furthering semi-automatically segment the starch granules, as
217 well as an inner and outer wall, based on their color veering (Supplementary Fig. 16).

218

219 ***Performance of resin-based microtechnique in different plant species and tissues***

220 The resin-based microtechnique produced comparable results between different
221 plant species and tissues. To test the versatility of the resin-based microtechnique and the
222 potential of histolomic analysis, we applied them to three C_3 plant leaves: *Arabidopsis*
223 *thaliana* (arabidopsis), *Triticum aestivum* (wheat), *Glycine Max* (soybean), and two C_4
224 plants leaves: *Zea mays* (maize) and *Amaranthus cruentus* (amaranth). Resin-based
225 microtechnique worked on all tissues, dye selectivity was the same as previously observed
226 for amaranth leaves, and randomness of iodine counterstaining was also observed.
227 Histolomic analysis revealed a number of similarities and differences between the leaf
228 sections: the same fundamental tissues but different morphology, morphometry and
229 composition (Supplementary Fig. 17 to 23). In order to deal with data and to obtain a
230 physiologically and evolutionarily meaningful value, we proposed a composite feature: the
231 "C_4 kranz level". This feature condensed some primary and derived morphometric and

232 compositional features, related to the C_4 Kranz anatomy[23] (Supplementary Fig. 24). *A.*
233 *thaliana* had the least developed C_4 Kranz anatomy and *A. cruentus* the most developed.
234 We also tested the resin-based microtechnique to follow histological changes during
235 germination and cotyledon maturation of amaranth seeds. The selectivity of the dyes was
236 the same as for leaves and revealed the development of organelles and cell wall
237 thickening (Supplementary Fig. 25 and 26). Finally, trichrome staining also worked on
238 paraffin sections, even without deparaffinization (Supplementary Fig. 27).
239
240 ***Trichrome staining and immunostaining of resin sections***
241 Trichrome staining can be used along with immunostaining on resin sections for
242 precise protein localization. We performed an immunostaining in an amaranth leaf section
243 to detect the RuBisCO large subunit (RbcL) responsible for carbon fixation. We used the
244 BCIP/NBT chromogen for signal development and then stained with trichrome staining.
245 BCIP/NBT gave an intense blue signal and did not interfere with the performance and hues
246 of the trichrome staining, resulting in a tetrachrome stain. Micrograph was segmented
247 based on the hue ranges of each dye, and protein and RbcL concentrations were
248 measured. RbcL was detected in almost all tissues, but mainly in the bundle sheath and
249 mesophyll. The bundle sheath contained about two times more RbcL than the mesophyll
250 (Fig. 6).
251
252 **DISCUSSION**
253 The resin-based microtechnique facilitated the dexterity-dependent steps and
254 offered advantages over the classic paraffin-based microtechnique. First, resin provided
255 mechanical support for the tissue in all steps, preventing breakage and scratching, and
256 preserving tissue structure better than paraffin (Supplementary video 1, and
257 Supplementary Fig. 11 and 27). Also, multiple thin and ultrathin sections can be obtained
258 simultaneously for light and electron microscopy analysis of the same cells, or for testing
259 multiple antibodies. Second, glass slide activation and gluing perfected the section
260 adhesion. Pirahna or sulphocromic activated and AES-glued slides eliminated section

261 detachment in all the slides that we used in this work (Fig. 1). Sections could only be
262 detached by deliberate scraping. This allows multiple analyses to be performed without
263 the risk of losing sections (Fig. 6). Due to the high toxicity of $Cr^{6+,}$ we recommend using
264 only the piranha solution for slides activation. On the other hand, it is worth to note that
265 classic microtechnique do not take into account the activation of slides and recommend a
266 short gluing time with AES[24], which in our experience did not work. Finally, the activation
267 also deeply cleans the slides, reducing wrinkles and artifacts caused by dirt
268 (Supplementary Fig. 7); however, there are also some drawbacks. Resin-based
269 microtechnique requires an ultramicrotome, which may not be available in some
270 laboratories. Despite thorough slide cleaning, resin sections naturally tend to wrinkle
271 during affixing as water evaporates, so the best affixed sections has to be selected.

272 Our trichrome staining method (Figure 3) significantly reduced steps, time,
273 reagents, toxicity, and variability compared to previous methods[6,11–14]. Classic staining
274 methods such as Johnanse's rely on multiple steps, repeated use of several reagents on
275 staining jars, and exposure to toxic or even explosive reagents such as picric acid[6]. Our
276 trichrome method reduced the 18 steps of the Johansen's method to 8 steps, the 2-48
277 hours to 5-10 min, and 6 reagents instead of 9. In addition, our trichrome method uses
278 small volumes of less toxic and more accessible reagents, making them easier to dispose
279 of, reducing variability due to repeated use (Supplementary Video 1).

280 Trichrome staining revealed the general molecular composition of the cell
281 structures. According to Johansen, fast green stains cytoplasm and cellulosic walls,
282 whereas safranin stains lignified and/or suberized walls, as well as nucleus and
283 chromosomes[6]. Precisely, fast green stains proteins and is even used to quantitatively
284 stain SDS-PAGE gels and nitrocellulose membranes[15,16]. Safranin stains lignin and suberin,
285 but its effectiveness in staining chromatin is not well-documented[17,25]. Iodine reacts with
286 various polysaccharides, showing the highest affinity for amylose[26,27]. So, trichrome
287 staining was consistent with the reported molecular specificity of the dyes, except for the
288 nucleus and chromatin. Overall, the nucleus, nucleolus, and heterochromatin stained
289 turquoise (Fig. 5). *T. aestivum* and *Z. mays* nuclei showed heterochromatin, but only those

290 of *T. aestivum* stained magenta (Supplementary Fig. 19 and 20). Safranin can interact with
291 DNA[28]. However, we found that safranin alone stained almost all tissue structures; its
292 specificity was defined by counterstaining with fast green (Supplementary Fig. 3 and 4).
293 Therefore, there should be specific molecules responsible for the safranin staining in *T.*
294 *aestivum* heterochromatin. Similarly, trichrome staining revealed stainable and non-
295 stainable starch granules. The amylose content could explain the differences. However,
296 the unstained granules were whiter and more electrolucent than the background in light
297 and electron microscopy respectively. On the other hand, the evidence is suggestive but
298 not conclusive if non-stained granules are the same as electrolucent granules. We can only
299 conclude that the amaranth leaf has two types of starch granules with different
300 compositions and interactions with LR white resin. Strikingly, both types can be formed in
301 the same chloroplast (Fig. 4).

302 Iodine counterstaining also differentiated the molecular composition of the cell
303 wall. It caused safranin-stained cell walls veering from magenta to reddish and orange
304 hues (Fig. 4). Our evidence suggests that this occurs gradually and selectively beginning in
305 the bundle sheath wall (Fig. 4) and continues until most of the wall of all tissues veers
306 (Supplementary Fig. 10). However, the epidermal wall showed an internal orange wall and
307 an external thicker magenta wall. Moreover, color segmentation showed that all cell walls
308 retained a small magenta portion (Supplementary Fig. 16). The cell wall consists of several
309 layers from the outside to the inside: middle lamella, primary wall, secondary wall, and
310 plasma membrane. The primary wall is composed of cellulose, hemicellulose, proteins,
311 and pectin; and the secondary wall is composed of cellulose, hemicellulose, and lignin[29].
312 The epidermal wall has additional outer layers of cutin and wax[30]. The primary wall is
313 about 0.1 µm thick, while the lignified secondary wall is thicker, about 2 to 10 µm[31]. Our
314 evidence suggests that safranin stains lignified and non-lignified walls, and that the orange
315 walls correspond to secondary walls (thicker) and the magenta walls to primary walls
316 (thinner). In addition, safranin stains lignin and suberin. Lignin can form complexes with
317 iodine, changing its UV-VIS absorption spectrum, while suberin interaction with iodine is
318 poorly understood[32–34]. The lignin-iodine reaction could cause the lignified secondary

319 walls veering while the non-lignified primary walls and the cutinized epidermal walls
320 remain magenta. Nevertheless, the ring structures of the tracheids are also lignified and
321 did not veer to orange hues[4] (Supplementary Fig. 10). Iodine counterstaining left several
322 questions about its reactions with starch granules and cell walls, as well as the
323 composition of these structures themselves. More research is needed to understand them
324 and also to reduce the randomness of iodine staining.

325 Our resin-based microtechnique resolved tissues, cells, organelles, and even
326 ultrastructural details, enabling large-scale histolomic analysis. The smaller resolved
327 ultrastructures were membranes within the bundle sheath vacuoles approximately ≈ 336-
328 560 nm thick (Supplementary Fig. 10). These membranes corresponded to cytosol
329 invaginations (310-900 nm thick) as proved by TEM microscopy (Fig. 5). The resolution of
330 widefield microscopy is limited to ≈ 200 nm in the X-Y axis (resolution), and 500–700 in the
331 z axis (depth of field)[35]. Resin-based microtechnique yielded ultrastructural detail close to
332 the resolution limit of widefield microscopy and close to the ultrastructural detail
333 provided by TEM microscopy at low magnifications (Fig. 5 and Supplementary Fig. 8-10). It
334 is in this "bridge" where the histolomic potential of the resin-based microtechnique lies:
335 to know a tissue in detail with TEM microscopy and then to analyze large areas at the
336 tissular, cellular and ultrastructural levels with light microscopy. It is conceptually similar
337 to correlative microscopy, but technically simpler and histologically more comprehensive.
338 On the other hand, we used resin sections about ≈500 nm thick to be within the depth of
339 field of widefield microscopy and to avoid interference from out-of-focus planes; the
340 essence of confocal microscopy. Thus, resin-based microtechnique complement the range
341 of high-resolution techniques that rely on fluorescent labeling, which tend to show only
342 what is immunolabeled and lose information from the rest of the tissue.

343 Histolomics requires a standardised strategy for micrograph analysis and
344 reporting. The nature of micrographs raises the need for an online platform with
345 interactive annotations for convenient sharing and tracking of plant tissue research
346 (Supplementary Fig. 11). On the other hand, colors in plant research are usually described
347 only by their "intuitive name". Accurate color description is important for micrograph

348 analysis. The RGB color space is widely used, even for lignin quantification[36]. However, the
349 HSB color space is the most intuitive and effectively separated the influence of dye (hue),
350 staining performance (saturation), and microscope setup (brightness) (Fig. 2). Hue
351 differences allowed segmentation of up to four cell structures, leaving some space in the
352 color wheel for more dyes. However, as with fluorescence microscopy, there is a risk of
353 color overlap[36], as was observed with cell walls and starch granules (Fig. 6).

354 Digital micrographs are data and should be analyzed beyond the naked eye. The
355 morphometric features were useful in quantifying the morphological differences between
356 C_3 and C_4 leaves, except for circularity, which did not show significant differences despite
357 being evident in the micrographs (Supplementary Fig. 22). Compositional features
358 revealed important physiological trends, such as the same protein concentration in young
359 and senescent amaranth leaves despite a reduction in proteoplasm content
360 (Supplementary Fig. 15). The primary and derived morphometric and compositional
361 features provide a basic description of the tissue, but can be selected, weighted, and
362 combined to investigate a particular phenomenon. At the "C_4 kranz level", we selected
363 primary and derived features related to the morphological traits of the C_4 Kranz
364 anatomy[23], weighted them according to their importance, and summed them to obtain a
365 score (Supplementary Fig. 24). This score condensed a complex micrograph, allowed
366 quantitative comparisons between plants, and could also be correlated with other
367 physiological or evolutionary issues such as carbon fixation efficiency or C_3-C_4 evolution.
368 Different combinations of primary and derived features can be used to quantitatively
369 study the effect of other phenomena such as biotic and abiotic stresses, genetic
370 mutations, nutrition, etc. on the phenotype of plant tissues.

371 In this work, we presented some primary, derived and composite features, but
372 more should be developed. Reliable and different cell shape formulas are needed, as
373 circularity failed. Positional features of cells and organelles will also be useful: e.g. the
374 position of organelles in bundle sheath cells to weigh their influence at the "C_4 kranz
375 level"; the position of organelles during cell division, among others. In addition, the tissue
376 area and the number of individual cells or organelles that can be measured are limited by

377 the need for time-consuming manual segmentation. Deep learning strategies should be
378 developed to automate micrograph segmentation and measurements of more individual
379 elements and larger areas to improve statistical power and leverage the resolution of
380 resin-based microtechnique.

381 Histolomics provided large-scale histologic descriptions, but took into account the
382 phenotypic individuality of each cell. In *A. thaliana* was observed a unique proteinaceous
383 cell vascular bundles (VBPC) with a smooth morphology and 26% of the protein content of
384 vascular bundles (Supplementary Fig. 17). This suggests a highly specialized function, and
385 although *A. thaliana* is the most studied plant, we could not find any information about
386 this cell. From ultrastructure to whole section, and from germination to senescence,
387 histolomics revealed histological similarities that species and tissues share, as well as
388 peculiarities that define them.

389 Histolomics challenged the C_4 category of the amaranth plant. RuBisCO fixes
390 carbon dioxide to form carbohydrates including starch. However, RuBisCO can also fix
391 oxygen, reducing the efficiency of carbon fixation. C_4 plants accumulate RuBisCO mainly in
392 bundle sheath cells, where carbon dioxide is enriched and thick lignified walls prevent
393 escape[23]. In amaranth leaves, we found increasing amounts of RbcL, starch granules, cell
394 wall thickness, and lignin concentration in palisade mesophyll, spongy mesophyll, and
395 bundle sheath. The amaranth leaf has an almost histolomically "perfect" Kranz anatomy,
396 but its RuBisCO have a distribution close to C_2 plants[23].

397 Omics have developed thanks to technological advances such as next-generation
398 sequencing and mass spectrometry[37], whereas plant histology still uses techniques that
399 are almost a century old[6]. In this work, plant microtechnique was reinvented to simplify its
400 methods and generate reproducible micrographs that allowed histolomic analysis. We
401 define histolomics as the large-scale, systematic, high-resolution microscopic study of
402 tissue composition, morphology, and morphometry from the ultrastructural to the whole
403 tissue level. Here we presented the first database of histolomes of plants commonly used
404 in research, obtaining data and images that make us rethink the perspective from which
405 we study life and its beauty.

406 **ONLINE METHODS**

407

408 **Glass slides preparation**

409 The glass slides treatments (2947-25X75, Corning) were performed in three steps:
410 washing, chemical activation, and silanization. Washing: glass slides were soaked in 2%
411 soap (Hyclin Plus Neutral, Hycel) for 30 min, and then both sides of each slide were
412 scrubbed with 15% soap with streak-free fiber (3068257, Scotch-Brite). They were rinsed
413 with tap water and then with Milli-Q water. Chemical activation: Six different solutions
414 were tested: MeOH:HCl 1:1 (MeOH-HCl); suflochromic mixture, $K_2Cr_2O_7$ ≈ 4% in
415 concentrated H_2SO_4 (H_2CrO_4); piranha solution, 30 ml concentrated H_2O_2 in 70 ml
416 concentrated H_2SO_4 (Piranha); glacial acetic acid (CH_3COOH); concentrated sulfuric acid
417 (H_2SO_4) or 1 M sodium hydroxide (NaOH). The sulfochromic mixture was prepared by
418 adding a little water to $K_2Cr_2O_7$ until a paste was made, and then the acid was added little
419 by little. Warning! All solutions are dangerous; particularly the sulfochromic mixture and
420 piranha solution are strong oxidizers and can react violently with organic material. In
421 addition, the sulfochromic mixture is highly toxic, so it must be handled with care and
422 disposed of according to your country's regulations. One group of slides was immersed in
423 staining jars for each of the solutions for 30 min at room temperature, and another was
424 kept without chemical activation (None). Slides were rinsed with Milli-Q water 3 times,
425 excess water was wrung out on a paper towel, and dried in an oven at 60 °C for 30 min.
426 Silanization: Dried slides were immersed in 4% (3-aminopropyl)triethoxysilane (AES,
427 440140, Sigma-Aldrich) solution in absolute ethanol for 1 h at room temperature, drained
428 and allowed to stand in 1 mM acetic acid in absolute ethanol for 10 min. They were rinsed
429 with Milli-Q water and dried as above, increasing the oven time at 60 °C to 1 h. It is
430 important that after the last rinse, the slides are kept in dust-free containers to avoid
431 artifacts in microscopy.

432 To evaluate the effectiveness of the activation, the contact angle of the slides with
433 water was measured. A slide was placed on a flat, level surface behind of a camera (T5i
434 with EF 100mm f/2.8L Macro IS USM lens, Canon) and in front of a backlit flash (newer S-

435 400N). 1 µL of Milli-Q water was added to the slide, allowed to stand for 30 s, and a
436 photograph was taken. The contact angle was measured on the photographs using the
437 ruler tool in Adobe Photoshop CS6.

438 To evaluate the effectiveness of silanization of the slides, their ability to retain a
439 resin section under strong washes was tested. Thin (500 nm) cross sections of *Amaranthus*
440 *cruentus* midrib were attached to each group of slides at 70°C for two minutes and
441 subjected to three aggressive washing procedures. First, they were digested with
442 proteinase K (10 µg/ml in PBS), denatured at 95°C for 2 min, and rinsed with a wash bottle
443 for 10 s. Second, they were heated in water at 95°C for 15 min, followed by rinsing with a
444 water jet for 10 s. Finally, they were subjected to heating in MeOH at 95°C for 3 min,
445 followed by rinsing with a water jet for 10 s. The sections were stained with safranin (0.5%
446 in water) and micrographs were taken. To prevent drying, the slides were covered with
447 the lid of a microtube during the incubation steps (See supplementary Video 1).

448

449 **Plant material**

450 Seeds of *Amaranthus cruentus* L cv. Amaranteca (Amaranth), *Arabidopsis thaliana*
451 (Arabidopsis), *Triticum aestivum* (Wheat), *Glycine max* (Soy bean), and *Zea mays* (Maize)
452 were germinated in 500 g of BM2 HP germination substrate (Berger, Saint-Modeste,
453 Quebec, CA). After 4 weeks, one leaf per plant was harvested. For *A. cruentus*, one leaf
454 was harvested at 4 weeks (young) and one at 8 weeks (senescent). In addition, during
455 germination of *A. cruentus*, seedlings were harvested at different stages: from seed to
456 seedling with mature cotyledons.

457

458 **General sample processing and microscopy**

459 Approximately 3 x 4 mm samples were taken from the midrib, a primary vein and
460 the leaf blade. In addition, one seed, one germinating seed, and complete cotyledons at
461 various stages of development were sampled from *A. cruentus*. Samples were fixed in 3%
462 glutaraldehyde, 2% formaldehyde, 0.5% Tween 20 in PBS (5 to 10 times the sample
463 volume) under vacuum for 20 min, and then shaken for 1 h, all on ice. Fixation was

464 continued overnight at 4°C and then rinsed three times with PBS while shaking for 1 hour
465 each time at room temperature. Samples were dehydrated in 30%, 50%, 70%, 95% and
466 absolute ethanol with shaking for 1 h at each step. Pre-inclusion in LR White
467 resin:absolute ethanol 1:1 with shaking was performed overnight, followed by inclusion in
468 pure resin (#14381, Electron Miscorscopy Sciences, PA, USA) another night. Pre-
469 embedding can be done in less time (4 h) for light dense samples such as leaves and
470 overnight for dense samples such as seeds. Usually, all samples were left overnight to
471 ensure complete and homogeneous resin penetration. Finally, samples were transferred
472 to gelatin capsules #2 (70103, Electron Miscorscopy Sciences, PA, USA) with pure resin
473 and polymerized at 55 °C for 48 h. For light and electron microscopy, thin and ultrathin
474 sections, respectively, were obtained (PowerTome PC RMC, Boeckeler Instruments). 3 x 4
475 mm samples can be difficult to handle; alternatively, slightly larger samples (≈ 5 x 6 mm)
476 can be obtained and the excess cut off with a scalpel or microscissors prior to
477 encapsulation. It is important that the sample does not exceed these dimensions so that it
478 can be positioned inside the capsule. Further details on embedding, sectioning and
479 staining are shown in Supplementary Video 1.

480 Thin sections were transferred to slides using a perfect loop, affixed in hotplate at
481 70 °C for 2 min and subjected to different procedures (described below). Finally,
482 micrographs were obtained with an Axio Imager M2 microscope (Zeiss) and a Canon T5i
483 camera. Ultrathin sections were placed on Formvar Carbon Support film, 150 Cupper
484 mesh (FCF-150 Cu) and counterstained with 2% uranyl acetate for 10 min, followed by 2%
485 lead citrate for 4 min. Samples were examined on a JEM-200 CX transmission electron
486 microscope (JEOL, Ltd.) at 100 kV equipped with a digital camera (SIA, Duluth).

487 For paraffin embedding, an *A. cruentus* leaf sample was fixed and dehydrated in
488 ethanol as described previously, but with two absolute ethanol steps. Sample was then
489 infiltrated in absolute alcohol:xylene 1:1 for 1 h, xylene for 1 h, xylene:paraffin (Tissue-Tek
490 VIP 4005 Embedding Medium, Sakura) 1:1 for 1 h at 60 °C, paraffin 1 for 1 h at 60 °C and
491 finally paraffin 2 for 1 h at 60°C. 10 µm sections (CUT 6062, SLEE, Nieder-Olm, Germany)

492 were obtained and placed in a water bath at 32 °C, collected on slides and affixed on
493 hotplate at 60 °C for 2 min. The sections were then stained and micrographs were taken.
494
495 **Staining**
496 Preliminary assays: Paradermal sections were stained with different methods.
497 Toluidine blue O (70103, Ted Pella, CA, SUA) for 5 min and rinse with water. Johansen's
498 method (Fig. 3a)[6]. Coomassie blue (Coomassie brilliant blue 0.025% in MeOH 40% Acetic
499 Acid 10%) for 5 min and rinse with water. Safranin (safranin O 1% in MeOH 40% and acetic
500 acid 10%) for 10 s, rinse with water, Coomassie blue for 10 s and rinse with water. Fast
501 green (fast green fcf 1% in 40% MeOH and 10% acetic acid) for 5 min, rinse with water,
502 Coomassie blue for 2'30'' and rinse with water. Finally, fast green for 5 min, rinse with
503 water, safranin for 5s and rinse with water. After the last water rinse, the slides were
504 dried on hotplate at 70 °C for 2 min and mounted with acrylic resin (Entellan, Merck) and a
505 coverslip.
506 Trichrome staining. The sections in Supplementary Figs. 4 to 6 were stained as
507 indicated in Fig. 3b, making modifications to the staining steps, order, and times as
508 indicated in each Figure. The sections in the remaining Figures (except Fig. 1 and 2) were
509 stained as indicated in Fig. 3b without modification.
510
511 **Immunohistochemical staining**
512 Resin sections were subjected to antigen retrieval with 100 µl of proteinase k at 50
513 µg/ml in PBS at 37°C for 30 min. The sections were then rinsed with TBST (Tris 20 mM,
514 NaCl 150 mM, Tween 20 1% pH 7.6). Blocking was performed with 200 µl of 1% BSA in
515 TBST (blocking solution) at 37 °C for 30 min. The blocking solution was removed and 200
516 µl of rabbit anti-RbcL (RuBisCO large subunit) antibody (Rabit anti-RbcL, Agrisera) diluted
517 1:500 in blocking solution was added. Sections were then incubated at 37 °C for 1 h, and
518 rinsed twice with TBST for 5 min each time. Alkaline phosphatase-conjugated goat anti-
519 rabbit antibody (200 µl) (Merk-Millipore) diluted 1:500 in blocking solution was added and
520 incubated at 37 °C for 30 min. Sections were rinsed twice with TBST and color developed

521 with fresh BCIP/NBT solution at 37 °C for 2 h. BCIP/NBT solution: 0.02% BCIP, 0.03% NBT,
522 in alkaline phosphatase buffer (100 mM Tris, 100 mM NaCl, 5 mM $MgCl_2$, 0.05% Tween 20
523 pH 9.5). Finally, the sections were rinsed twice with TBST, twice with Milli-Q water, and
524 dried on hotplate at 70 °C for 2 min. A negative control was performed without the anti-
525 RbcL antibody, and a positive sample was stained with trichrome staining. Incubation
526 steps were performed by covering the section with a microtube lid, as shown in
527 Supplementary Video 1.
528
529 **Color measurement**
530 Different areas (n=30) of the micrographs were measured with the Adobe
531 Photoshop CS6 "eyedropper" tool with a sample size of 3 x 3 pixels, and statistical analysis
532 was performed with GraphPad Prism 9.
533
534 **Semi-automatic image segmentation with Matlab R2024a**
535 The micrographs were segmented using the "Color Tresholder" tool in the "HSV"
536 color space. The segmented images were exported in black and white. To make accurate
537 adjustments, the HSV values were monitored in the segmentation function, and the
538 sliders were adjusted until the desired values were obtained. Images were exported at a
539 resolution close to the original micrograph (See supplementary video 1).
540
541 **Manual image segmentation and morphometric and compositional measurement with**
542 **Adobe Photoshop CS6**
543 Morphometric analysis. A micrograph layer with a layer mask was generated for
544 each element to be measured. The density of the mask was adjusted to 50% and each
545 element was manually contoured with the brush tool. The workspace was calibrated using
546 the "set scale to size" tool and the micrograph scale bar. The selections of each element to
547 be analyzed were retrieved through the layer masks and measured with the "record
548 measurements" function. The data were exported and analyzed with GraphPad Prism 9.

Compositional analysis by densitometric analysis of lignin, proteins and immunolabel. The micrograph was converted to grayscale/negative, and a baseline adjustment was performed. The black and white segmented image was resized to the size of the micrograph and used as a mask. Finally, image analysis was performed on the masked grayscale/negative micrograph and the data was saved for statistical analysis in GraphPad Prism 9.

A detailed tutorial on image segmentation and analysis using Matlab and Adobe Photoshop CS6 is shown in the second part of Supplementary Video 1.

Supplementary information

Supplementary video 1: https://www.youtube.com/watch?v=di2SDqe49rY

Acknowledgments

Ivan Takeshi Cerritos Castro thanks to CONACYT fellowship 719217, and the grant CNCA.FONCA.04S.04.ACT.PR.ACT.178.18. from the National Fund for Culture and Arts (FONCA), Mexico. The authors thank to Laboratory for Nanoscience and Nanotechnology Research, LINAN, IPICYT.

Author contributions

Ivan Takeshi Cerritos-Castro: Conceptualization, investigation, fund acquisition, methodology, and writing the original draft. **Olga Araceli Patrón-Soberano:** Investigation, methodology, review and editing. **Ana Paulina Barba de la Rosa:** Supervision, funds, resources, review, and editing.

Competing financial interest

The authors declare no competing financial interests.

579 **FIGURE CAPTIONS**

580

581 **Figure 1. Activation and gluing treatments increase the wettability and adhesiveness of**
582 **glass slides.**

583 a Contact angle photographs after chemical activation and gluing (silanization). b Resin
584 sections in the different slides after strong washing. Arrows indicate detachments. Scale
585 bar = 500 µm. c Contact angle mean (n=3) ± SD. One-way ANOVA and Holm-Šídák's post-
586 tests were performed, letters indicate significant differences at $p<0.01$. Activation
587 treatment is indicated at the top. Activation creates hydroxyl groups that make the glass
588 hydrophilic, causing water droplets to spread widely (wettability) and reducing the contact
589 angle. The hydroxyl groups then react with the AES during the gluing process, improving
590 the adhesiveness of the glass.

591

592 **Figure 2. Classic Johansen's staining does not work on resin sections.**

593 a Light micrographs of *A. cruentus* leaf paradermal sections stained with different
594 methods. Scale bar = 50 µm. b Violin plots (n=30) with median, interquartile range and
595 hue ranges (filled, only for saturation ≤ 15%) observed in cell wall (CW), protoplasm (PR)
596 and background (BK). Kruskal-Wallis ANOVA and Dunn's post-test were performed;
597 differences are shown at $p<0.01$. HSB graphs correspond to the top micrograph.

598 Hue (H) represents the visible light spectrum on the color wheel, with values ranging from
599 0 to 360°. Saturation indicates the amount of color and brightness the amount of light,
600 and their values range from 0 to 100%. Low saturation tends to gray and high saturation
601 tends to vivid colors. Low brightness tends to black and high brightness tends to white.
602 The hue depended on the dye, the saturation on the staining performance, and the
603 brightness on the illumination settings of the microscope and camera (standardized).

604

605 **Figure 3. Reinvented Johansen's staining for resin sections and made it trichrome.**

606 **a** Johansen's 1940 staining method with safranin and fast green for paraffin sections. **b**
607 Trichrome staining method with fast green, safranin, and Lugol's iodine for both paraffin

608 and acrylic resin sections. The Johansen method has been a reference in plant histology
609 since 1940. It requires many steps, time, and toxic, explosive, and expensive reagents.
610 Johansen's method did not work on resin sections, so we completely reformulated its dyes
611 and steps, and added Lugol's iodine. The trichrome method greatly reduced the steps,
612 time, toxicity, added a new dye, and worked on both resin and paraffin sections.
613
614 **Figure 4. Trichrome staining differentiates cellular composition beyond Johansen's dyes.**
615 **a** Light micrograph of a cross-section of *A. cruentus* leaf stained with trichrome staining.
616 Arrows indicate the hue range of some structures. **b** Violin plots (n=30) with median,
617 interquartile range, data distribution (circles), and hue range observed in the epidermal
618 wall (E-CW), the mesophyll wall (M-CW), bundle sheath wall (B-CW), bundle sheath
619 proteoplasm (B-PT), mesophyll proteoplasm (M-PT), mesophyll starch granules (M-ST),
620 and bundle sheath starch granules (B-ST). **c** Enlargement of the white box in a. Mauve
621 arrows point to stained and white arrows to unstained granules. d TEM of an *A. cruentus*
622 leaf cross section. Mauve arrows point to electrodense granules and white arrows to
623 electrolucent granules. ST, starch; CL, chloroplast; CW, cell wall; MI, mitochondrion; NU,
624 nucleus; and NL, nucleolus. Addition of iodine counterstaining to a tissue stained with
625 Johansen's dyes caused hue changes (veering). Veering occurred mainly in the CW in a
626 tissue-dependent manner. M-CW hardly veered, E-CW veered to reddish, and B-CW
627 veered to reddish and even orange hues, suggesting compositional differences in their cell
628 walls. The proteoplasm, on the other hand, showed no significant veering between
629 tissues. Finally, some ST stained mauve, while others remained white, even whiter than
630 the background itself. This pattern was repeated when the section was examined by TEM,
631 suggesting compositional differences in the starch granules.
632
633 **Figure 5. Resin-based microtechnique allows light microscopy to resolve structures that**
634 **would normally require TEM.**
635 Digitally isolated bundle sheath cells from light and electron micrographs (not the same
636 cell), from a young (4 weeks), and a senescent (8 weeks) *A. cruentus* leaf. Scale bar= 5 µm.

637 High-resolution light micrographs revealed several organelles and ultrastructures that
638 were identified by TEM. The characteristic cell wall thinning of PITS was observed in the
639 bundle sheath-mesophyll cell junctions. Vacuoles were easily identified by their lack of
640 color and texture; however, some cytoplasmic invaginations were detected. All
641 proteoplasm stained turquoise, but saturation differences revealed several organelles and
642 cytosol. Although these structures were not sharply resolved by light microscopy, it was
643 sufficient to identify them and follow their behavior during the senescence process. The
644 senescent cell has lost its cytoplasm, its chloroplasts have lost their centripetal position,
645 contain more starch and are undergoing degradation, but the cell still retains the nucleus
646 and nucleolus. This behavior can be distinguished by both optical and TEM microscopy.
647
648 **Figure 6. Trichrome staining and immunostaining revealed the precise localization of**
649 **RbcL in cells and organelles.**
650 Light micrographs of *A. cruentus* leaf sections immunostained for RbcL. **a** No signal was
651 observed in the negative control. **b** RbcL and background (BK) signal was observed in the
652 anti-RbcL sample. **c** Trichrome staining stained the starch but did not cause significant
653 veering in the cell wall. **d** The combination of immunostaining and trichrome staining
654 summed the colors of both techniques without affecting each other. AE, adaxial
655 epidermis; PM, palisade mesophyll; VB, vascular bundles; BS, bundle sheath; SM, spongy
656 mesophyll; BE, abaxial epidermis. To differentiate the immunostaining signal: a weak
657 signal outside the proteoplasm was considered as background and a strong signal inside
658 the proteoplasm as RbcL. Tetrachrome staining (**d**) facilitated this differentiation by
659 showing the immunostaining signal and the stained tissue, in contrast to (**b**) where the
660 tissue lacks contrast. **e-h** Color segmentation of (**d**) showing separately the cellular
661 elements and the RbcL signal. **i** Violin plots (n=30) with median, interquartile range, and
662 observed color range. Kruskal-Wallis ANOVA and Dunn's post-test were performed;
663 differences are shown with $p<0.01$. Although there were significant differences, the hue
664 ranges overlapped, so in practice they were adjusted (in Matlab) to intermediate values

665 for color segmentation (**j**). Densitometric analysis showed the highest RbcL content in the
666 BS, but similar concentrations in all tissues (**l**).
667
668 **REFERENCES**

669 1. Zivy, M. *et al.* The quest for tolerant varieties: the importance of integrating
670 "omics" techniques to phenotyping. *Front. Plant Sci.* **6**, (2015).
671 2. Xu, H. & Bassel, G. W. Linking Genes to Shape in Plants Using Morphometrics. *Annu.*
672 *Rev. Genet.* **54**, 417–437 (2020).
673 3. Millar, A. H., Carrie, C., Pogson, B. & Whelan, J. Exploring the Function-Location
674 Nexus: Using Multiple Lines of Evidence in Defining the Subcellular Location of Plant
675 Proteins. *Plant Cell* **21**, 1625–1631 (2009).
676 4. Taylor, T. N., Taylor, E. L. & Krings, M. 7 - Introduction to Vascular Plant Morphology
677 and Anatomy. in (eds. Taylor, T. N., Taylor, E. L. & Krings, M. B. T.-P. (Second E.)
678 201–222 (Academic Press, 2009). doi:https://doi.org/10.1016/B978-0-12-373972-
679 8.00007-3.
680 5. McCann, M. T., Ozolek, J. A., Castro, C. A., Parvin, B. & Kovacevic, J. Automated
681 Histology Analysis: Opportunities for signal processing. *IEEE Signal Process. Mag.*
682 **32**, 78–87 (2015).
683 6. Johansen, D. A. *Plant microtechnique*. (McGraw-Hill Book company, Inc., 1940).
684 7. Labit, H. *et al.* A simple and optimized method of producing silanized surfaces for
685 FISH and replication mapping on combed DNA fibers. *Biotechniques* **45**, 649–658
686 (2008).
687 8. Han, Y., Mayer, D., Offenhäusser, A. & Ingebrandt, S. Surface activation of thin
688 silicon oxides by wet cleaning and silanization. *Thin Solid Films* **510**, 175–180 (2006).
689 9. Jakša, G., Štefane, B. & Kovač, J. Influence of different solvents on the morphology
690 of APTMS-modified silicon surfaces. *Appl. Surf. Sci.* **315**, 516–522 (2014).
691 10. Agnihotri, S., Mukherji, S. & Mukherji, S. Immobilized silver nanoparticles enhance
692 contact killing and show highest efficacy: elucidation of the mechanism of
693 bactericidal action of silver. *Nanoscale* **5**, 7328 (2013).

694 11. O'Brien, T. P. & McCully, M. E. *The Study of plant structure : principles and selected*
695 *methods*. (Termarcarphi Pty. Ltd, 1981).
696 12. Ma, Y., Sawhney, V. K. & Steeves, T. A. Staining of paraffin-embedded plant material
697 in safranin and fast green without prior removal of the paraffin. *Can. J. Bot.* **71**,
698 996–999 (1993).
699 13. Fowke, L. C. & Rennie, P. J. Botanical Microtechnique for Plant Cultures. in *Plant*
700 *Cell, Tissue and Organ Culture* 217–228 (Springer Berlin Heidelberg, 1995).
701 doi:10.1007/978-3-642-79048-5_17.
702 14. Zenchyzen, B. *et al.* Comparative Nectary Morphology across Cleomaceae
703 (Brassicales). *Plants* **12**, 1263 (2023).
704 15. Kurien, B. T. & Scofield, R. H. Ultrarapid Electrophoretic Transfer of High and Low
705 Molecular Weight Proteins Using Heat. in 181–190 (2009). doi:10.1007/978-1-
706 59745-542-8_20.
707 16. Bertolini, M. J., Tankersley, D. L. & Schroeder, D. D. Staining and destaining
708 polyacrylamide gels: A comparison of Coomassie blue and fast green protein dyes.
709 *Anal. Biochem.* **71**, 6–13 (1976).
710 17. Kitin, P., Nakaba, S., Hunt, C. G., Lim, S. & Funada, R. Direct fluorescence imaging of
711 lignocellulosic and suberized cell walls in roots and stems. *AoB Plants* **12**, plaa032
712 (2020).
713 18. Koga, D., Kusumi, S., Shodo, R., Dan, Y. & Ushiki, T. High-resolution imaging by
714 scanning electron microscopy of semithin sections in correlation with light
715 microscopy. *Microscopy* **64**, 387–394 (2015).
716 19. Kaplan, D. R. The science of plant morphology: definition, history, and role in
717 modern biology. *Am. J. Bot.* **88**, 1711–1741 (2001).
718 20. Ashburner, J. & Ridgway, G. R. Tensor-Based Morphometry. in *Brain Mapping* 383–
719 394 (Elsevier, 2015). doi:10.1016/B978-0-12-397025-1.00309-2.
720 21. Vu, Q. D. *et al.* Methods for Segmentation and Classification of Digital Microscopy
721 Tissue Images. *Front. Bioeng. Biotechnol.* **7**, (2019).
722 22. Khoshravesh, R., Stata, M., Adachi, S., Sage, T. L. & Sage, R. F. Evolutionary

723 Convergence of C4 Photosynthesis: A Case Study in the Nyctaginaceae. *Front. Plant*
724 *Sci.* **11**, (2020).
725 23. Sage, R. F., Khoshravesh, R. & Sage, T. L. From proto-Kranz to C4 Kranz: building the
726 bridge to C4 photosynthesis. *J. Exp. Bot.* **65**, 3341–3356 (2014).
727 24. Bagasra, O. Protocols for the in situ PCR-amplification and detection of mRNA and
728 DNA sequences. *Nat. Protoc.* **2**, 2782–95 (2007).
729 25. Smith, K., Steinberger, A. & Perloff, W. SAFRANIN AS A STAIN FOR CHROMOSOMES.
730 *Lancet* **281**, 1379–1380 (1963).
731 26. Jideani, I. A., Takeda, Y. & Hizukuri, S. Structures and physicochemical properties of
732 starches from acha (Digitaria exilis), iburu (D. iburua), and tamba (Eleusine
733 coracana). *Cereal Chem.* **73**, 677–685 (1996).
734 27. Hubbe, M. A., Chandra, R. P., Dogu, D. & van Velzen, S. T. J. Analytical staining of
735 cellulosic materials: A Review. *BioResources* **14**, 7387–7464 (2019).
736 28. Long, J., Wang, X., Xu, D. & Ding, L. Spectroscopic studies on the interaction
737 mechanisms of safranin T with herring sperm DNA using acridine orange as a
738 fluorescence probe. *J. Mol. Recognit.* **27**, 131–137 (2014).
739 29. Loix, C. *et al.* Reciprocal Interactions between Cadmium-Induced Cell Wall
740 Responses and Oxidative Stress in Plants. *Front. Plant Sci.* **8**, (2017).
741 30. Chen, H. & Wang, L. Pretreatment Strategies for Biochemical Conversion of
742 Biomass. in *Technologies for Biochemical Conversion of Biomass* 21–64 (Elsevier,
743 2017). doi:10.1016/B978-0-12-802417-1.00003-X.
744 31. Megías, P. M. Atlas of plant and animal histology. *Universidad De Vigo*
745 https://mmegias.webs.uvigo.es/02-english/5-celulas/ampliaciones/2-pared-
746 celular.php (2023).
747 32. Deng, Y. *et al.* Investigation of aggregation and assembly of alkali lignin using iodine
748 as a probe. *Biomacromolecules* **12**, 1116–25 (2011).
749 33. Kosma, D. K. *et al.* At <scp>MYB</scp> 41 activates ectopic suberin synthesis and
750 assembly in multiple plant species and cell types. *Plant J.* **80**, 216–229 (2014).
751 34. Scott, F. M. Internal Suberization of Tissues. *Bot. Gaz.* **111**, 378–394 (1950).

752 35. Sims, J., Schlögelhofer, P. & Kurzbauer, M.-T. From Microscopy to Nanoscopy:
753 Defining an Arabidopsis thaliana Meiotic Atlas at the Nanometer Scale. *Front. Plant*
754 *Sci.* **12**, (2021).
755 36. Liao, K. *et al.* A novel in-situ quantitative profiling approach for visualizing changes
756 in lignin and cellulose by stained micrographs. *Carbohydr. Polym.* **297**, 119997
757 (2022).
758 37. Dai, X. & Shen, L. Advances and Trends in Omics Technology Development. *Front.*
759 *Med.* **9**, (2022).
760

PLANT MICROTECHNIQUE WITH RESIN - TOWARDS PLANT HISTOLOMICS

Ivan T. Cerritos-Castro[1], Araceli Patrón-Soberano[1], Ana P. Barba de la Rosa[1*].

[1]Molecular Biology Division, Instituto Potosino de Investigación Científica y Tecnológica A.C., IPICYT, San Luis Potosí, México.

FIGURES

The images are high resolution, please zoom in to see the details.

GRAPHICAL ABSTRACT

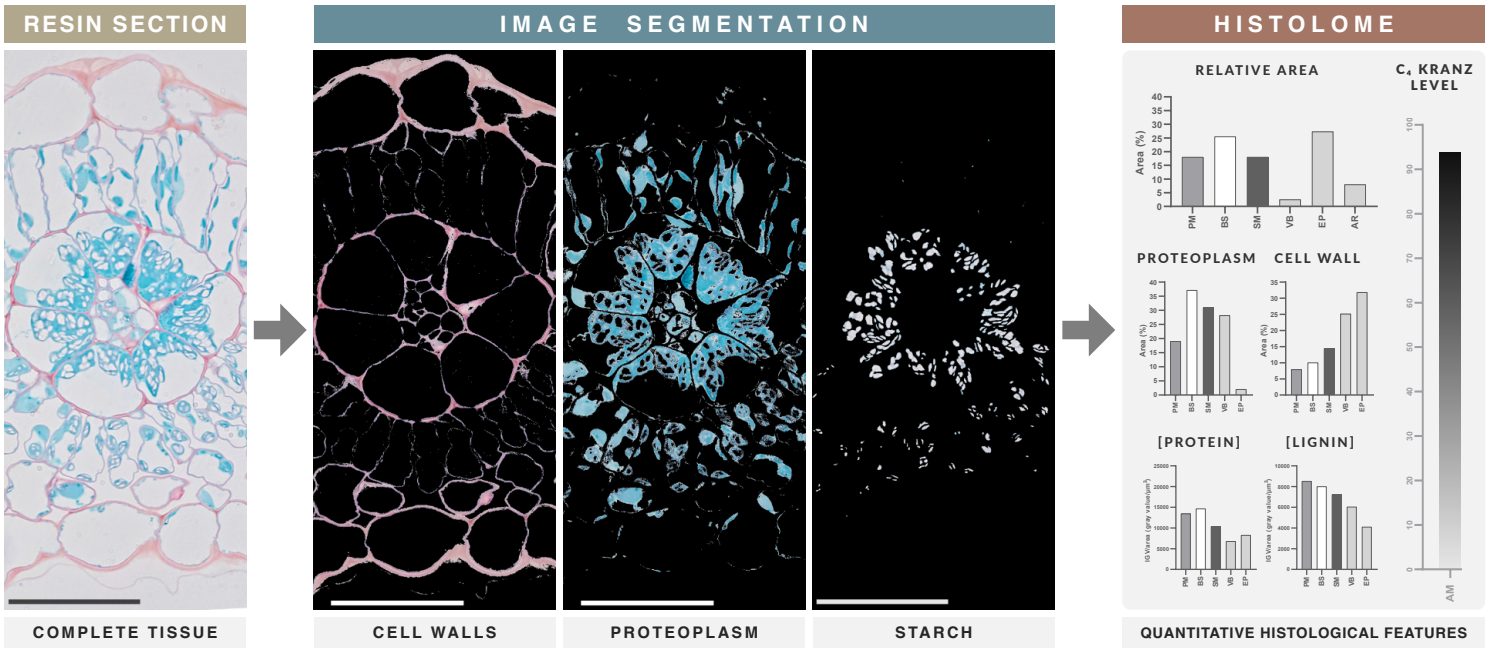

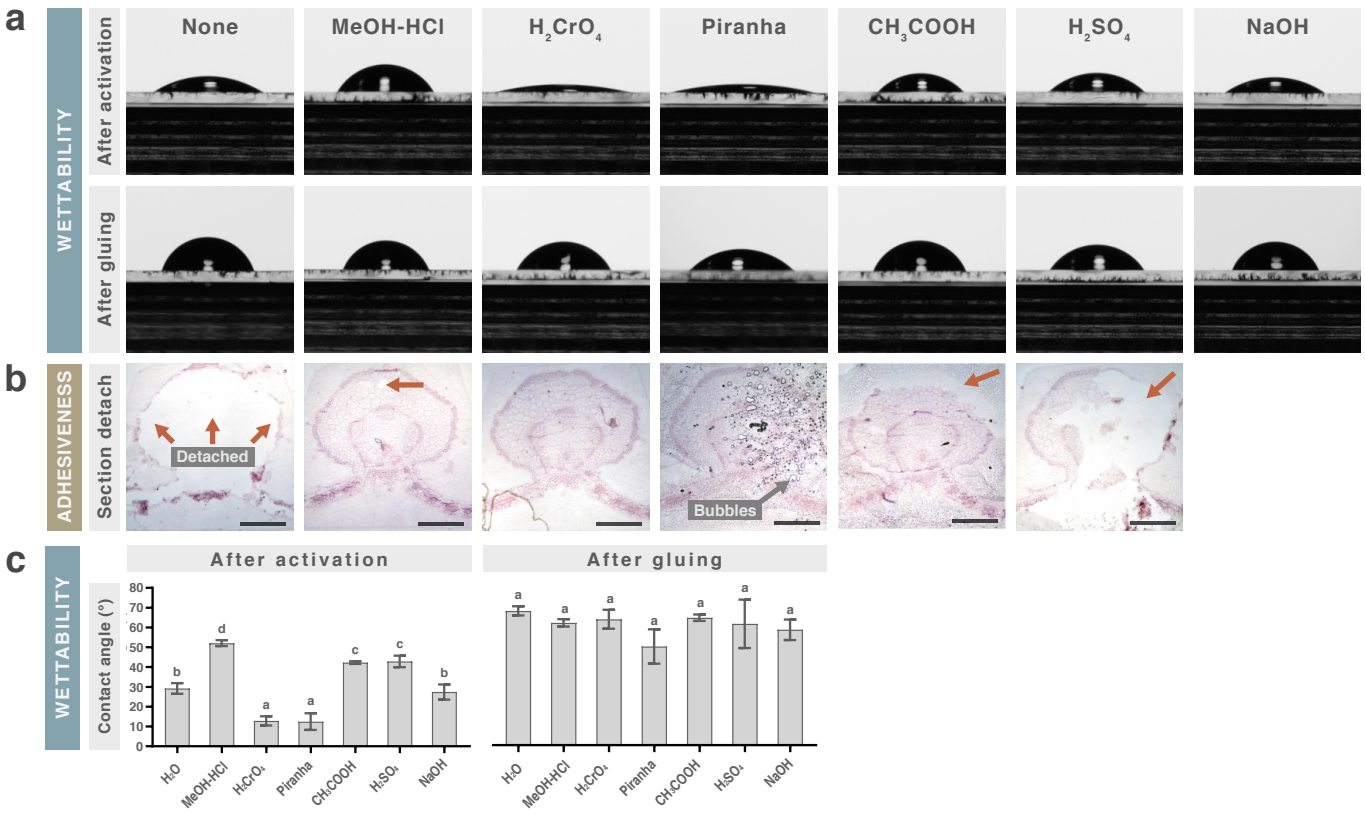

FIGURE 1 **Activation and gluing treatments increase the wettability and adhesiveness of glass slides**

a Contact angle photographs after chemical activation and gluing (silanization). **b** Resin sections in the different slides after strong washing. Arrows indicate detachments. Scale bar = 500 μm. **c** Contact angle mean (n=3) ± SD. One-way ANOVA and Holm-Šídák's post-tests were performed, letters indicate significant differences at $p<0.01$. Activation treatment is indicated at the top. Activation creates hydroxyl groups that make the glass hydrophilic, causing water droplets to spread widely (wettability) and reducing the contact angle. The hydroxyl groups then react with the AES during the gluing process, improving the adhesiveness of the glass.

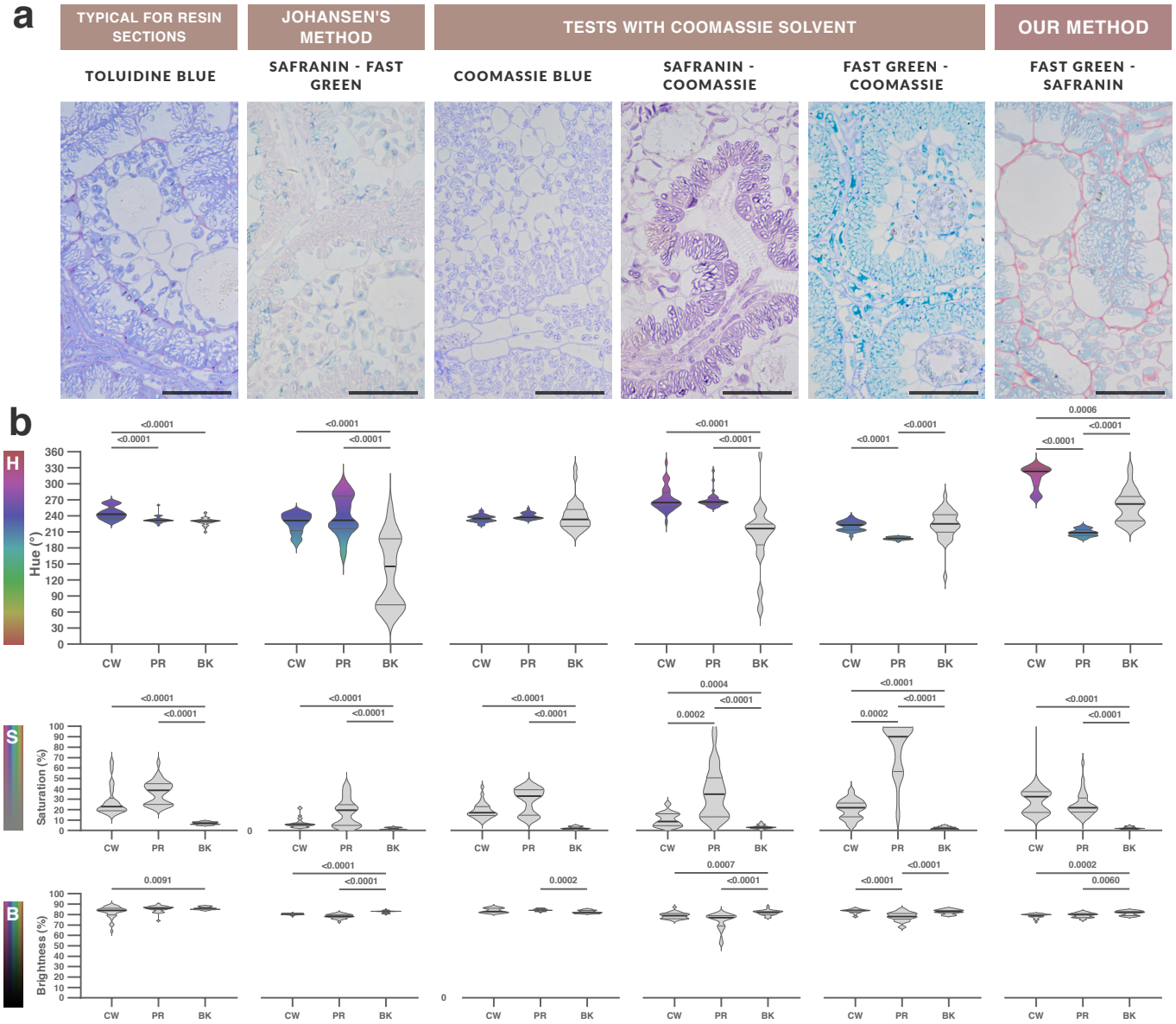

FIGURE 2 **Classic Johansen's staining does not work on resin sections**

a Light micrographs of *A. cruentus* leaf paradermal sections stained with different methods. Scale bar = 50 μm. **b** Violin plots (n=30) with median, interquartile range and hue ranges (filled, only for saturation ≤ 15%) observed in cell wall (CW), protoplasm (PR) and background (BK). Kruskal-Wallis ANOVA and Dunn's post-test were performed, differences are shown at $p<0.01$. HSB graphs correspond to the top micrograph. Hue (H) represents the visible light spectrum on the color wheel, with values ranging from 0 to 360°. Saturation indicates the amount of color and brightness the amount of light, and their values range from 0 to 100%. Low saturation tends to gray and high saturation tends to vivid colors. Low brightness tends to black and high brightness tends to white. The hue depended on the dye, the saturation on the staining performance, and the brightness on the illumination settings of the microscope and camera (standardized).

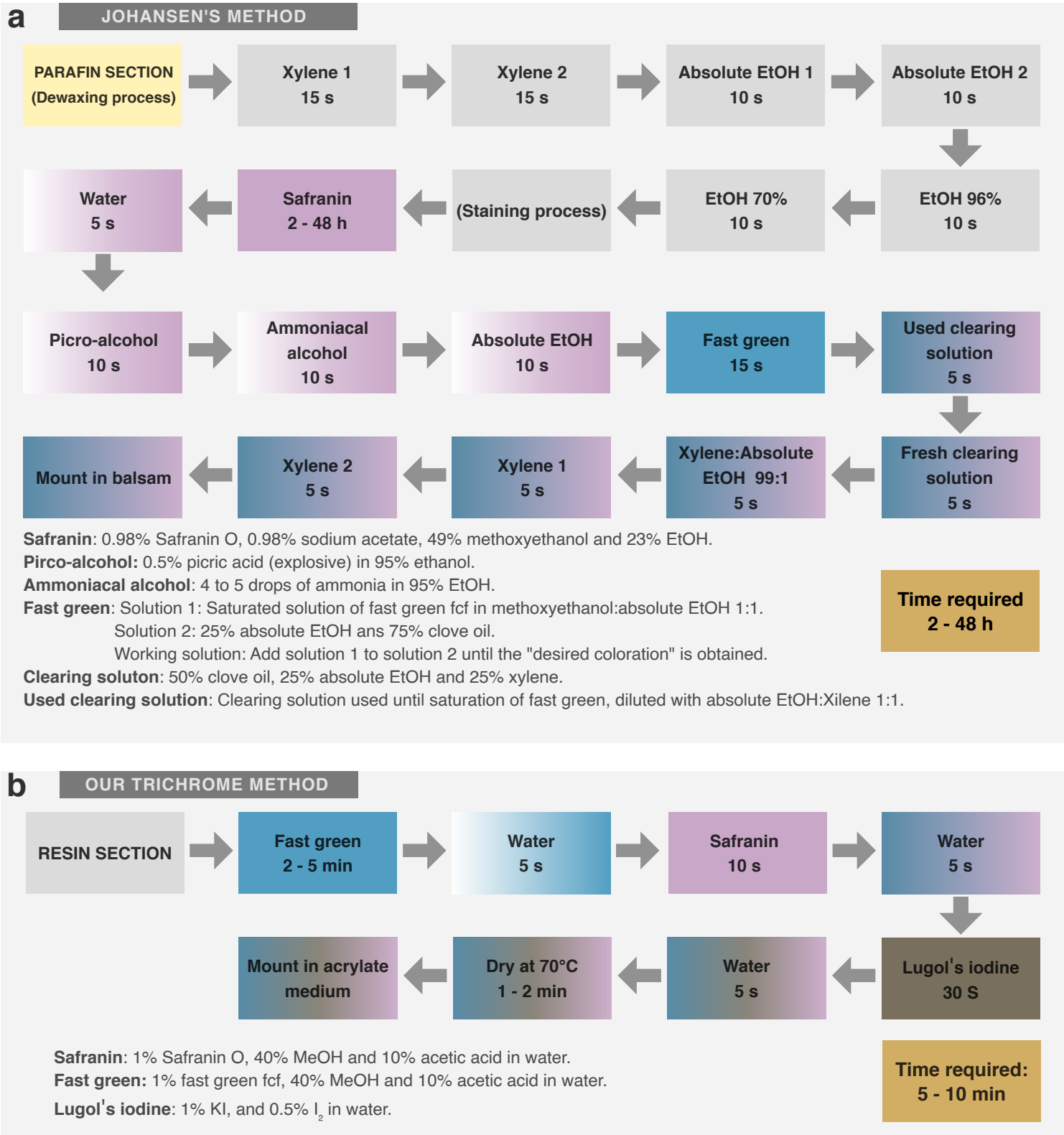

FIGURE 3 **We reinvented Johansen's staining for resin sections and made it trichrome**

a Johansen's 1940 staining method with safranin and fast green for paraffin sections. **b** Trichrome staining method with fast green, safranin, and Lugol's iodine for both paraffin and acrylic resin sections. The Johansen method has been a reference in plant histology since 1940. It requires many steps, time, and toxic, explosive, and expensive reagents. Johansen's method did not work on resin sections, so we completely reformulated its dyes and steps, and added Lugol's iodine. The trichrome method greatly reduced the steps, time, toxicity, added a new dye, and worked on both resin and paraffin sections.

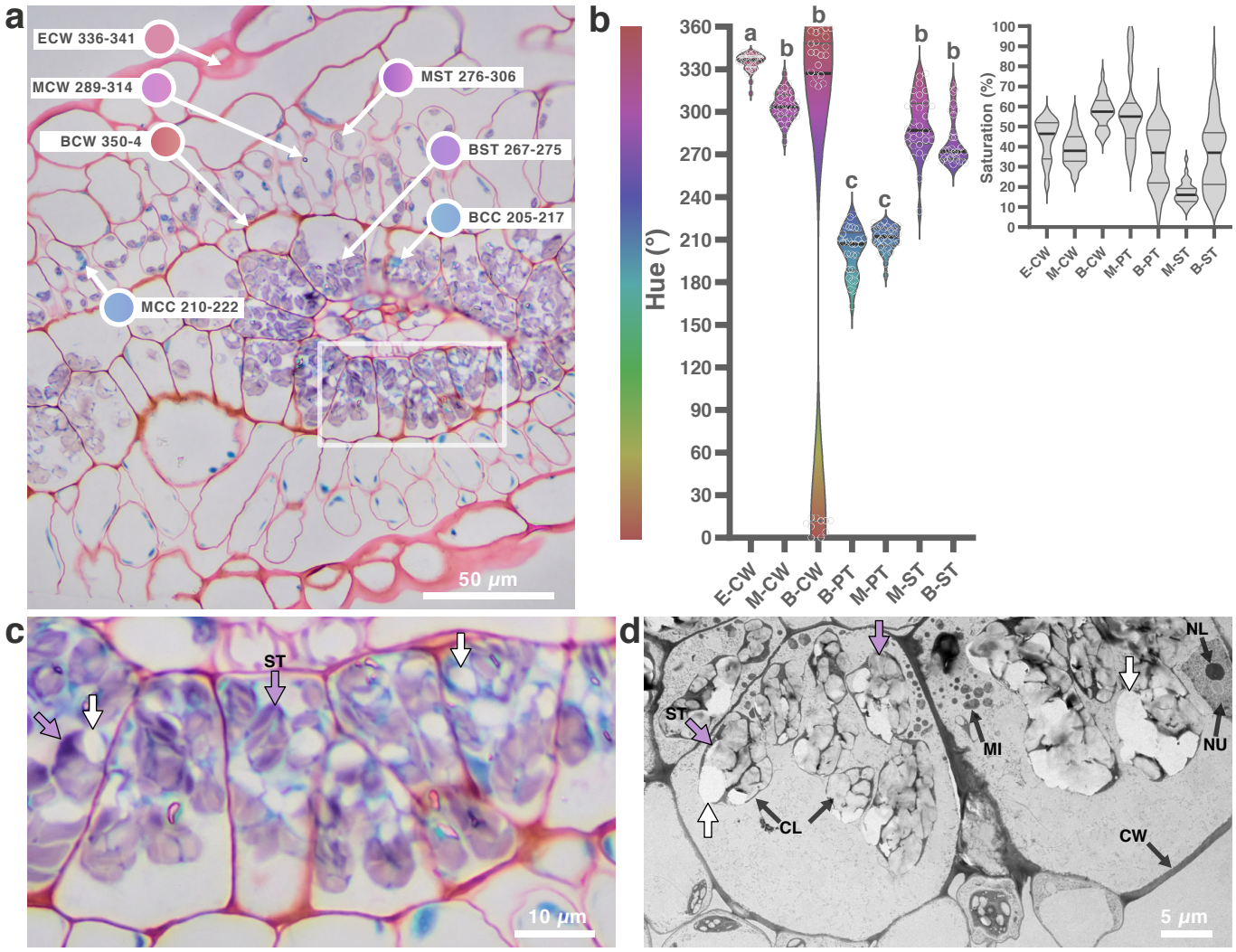

FIGURE 4 **Trichrome staining differentiates cellular composition beyond Johansen's dyes**

a Light micrograph of a cross-section of *A. cruentus* leaf stained with trichrome staining. Arrows indicate the hue range of some structures. **b** Violin plots (n=30) with median, interquartile range, data distribution (circles), and hue range observed in the epidermal wall (E-CW), the mesophyll wall (M-CW), bundle sheath wall (B-CW), bundle sheath proteoplasm (B-PT), mesophyll proteoplasm (M-PT), mesophyll starch granules (M-ST), and bundle sheath starch granules (B-ST). **c** Enlargement of the white box in a. Mauve arrows point to stained and white arrows to unstained granules. **d** TEM of an *A. cruentus* leaf cross section. Mauve arrows point to electrodense granules and white arrows to electrolucent granules. ST, starch; CL, chloroplast; CW, cell wall; MI, mitochondrion; NU, nucleus; and NL, nucleolus. Addition of iodine counterstaining to a tissue stained with Johansen's dyes caused hue changes (veering). Veering occurred mainly in the CW in a tissue-dependent manner. M-CW hardly veered, E-CW veered to reddish, and B-CW veered to reddish and even orange hues, suggesting compositional differences in their cell walls. The proteoplasm, on the other hand, showed no significant veering between tissues. Finally, some ST stained mauve, while others remained white, even whiter than the background itself. This pattern was repeated when the section was examined by TEM, suggesting compositional differences in the starch granules.

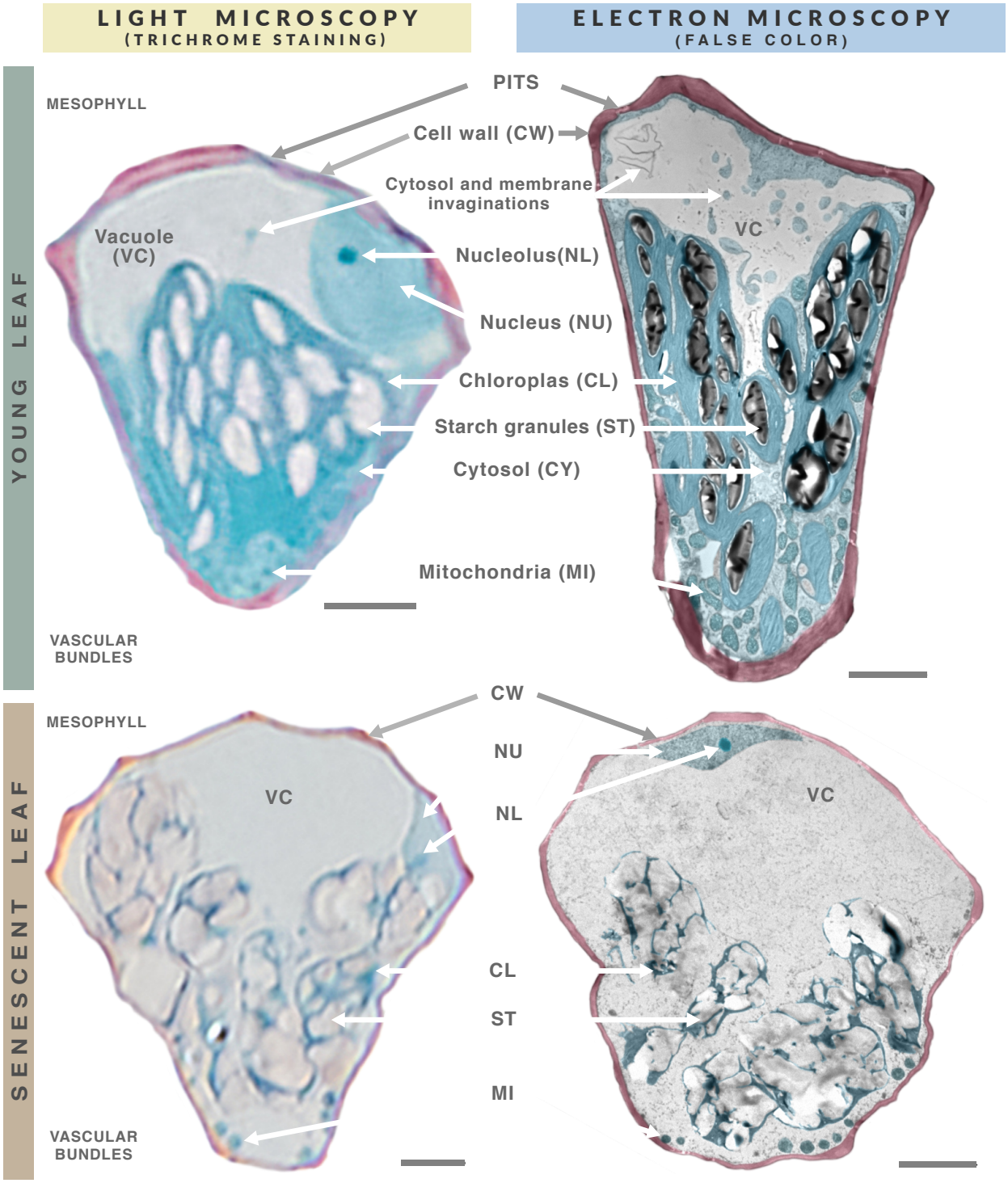

FIGURE 5 **Resin-based microtechnique allows light microscopy to resolve structures that would normally require TEM**

Digitally isolated bundle sheath cells from light and electron micrographs (not the same cell), from a young (4 weeks), and a senescent (8 weeks) *A. cruentus* leaf. Scale bar= 5 μm. High resolution light micrographs revealed several organelles and ultrastructures that were identified by TEM. The characteristic cell wall thinning of PITS was observed in the bundle sheath-mesophyll cell junctions. Vacuoles were easily identified by their lack of color and texture; however, some cytoplasmic invaginations were detected. All proteoplasm stained turquoise, but saturation differences revealed several organelles and cytosol. Although these structures were not sharply resolved by light microscopy, it was sufficient to identify them and follow their behavior during the senescence process. The senescent cell has lost its cytoplasm, its chloroplasts have lost their centripetal position, contain more starch and are undergoing degradation, but the cell still retains the nucleus and nucleolus. This behavior can be distinguished by both optical and TEM microscopy.

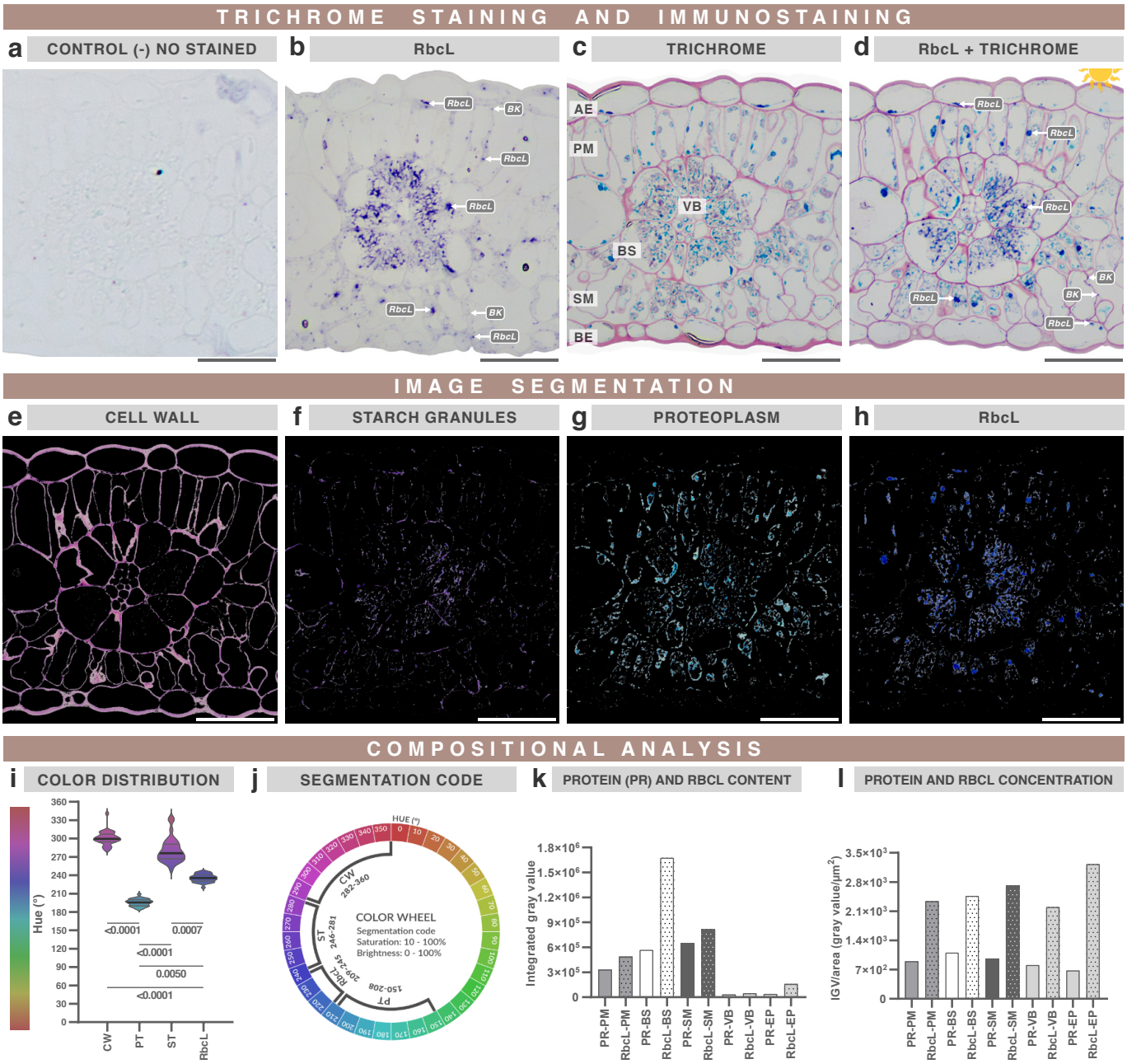

FIGURE 6 **Trichrome staining and immunostaining revealed the precise localization of RbcL in cells and organelles**

Light micrographs of *A. cruentus* leaf sections immunostained for RbcL. **a** No signal was observed in the negative control. **b** RbcL and background (BK) signal was observed in the anti-RbcL sample. **c** Trichrome staining stained the starch but did not cause significant veering in the cell wall. **d** The combination of immunostaining and trichrome staining summed the colors of both techniques without affecting each other. AE, adaxial epidermis; PM, palisade mesophyll; VB, vascular bundles; BS, bundle sheath; SM, spongy mesophyll; BE, abaxial epidermis. To differentiate the immunostaining signal: a weak signal outside the proteoplasm was considered as background and a strong signal inside the proteoplasm as RbcL. Tetrachrome staining (d) facilitated this differentiation by showing the immunostaining signal and the stained tissue, in contrast to (b) where the tissue lacks contrast. **e-h** Color segmentation of (d) showing separately the cellular elements and the RbcL signal. **i** Violin plots (n=30) with median, interquartile range, and observed color range. Kruskal-Wallis ANOVA and Dunn's post-test were performed, differences are shown with $p<0.01$. Although there were significant differences, the hue ranges overlapped, so in practice they were adjusted (in Matlab) to intermediate values for color segmentation (**j**). Densitometric analysis showed the highest RbcL content in the BS (**k**), but similar concentrations in all tissues (**l**).

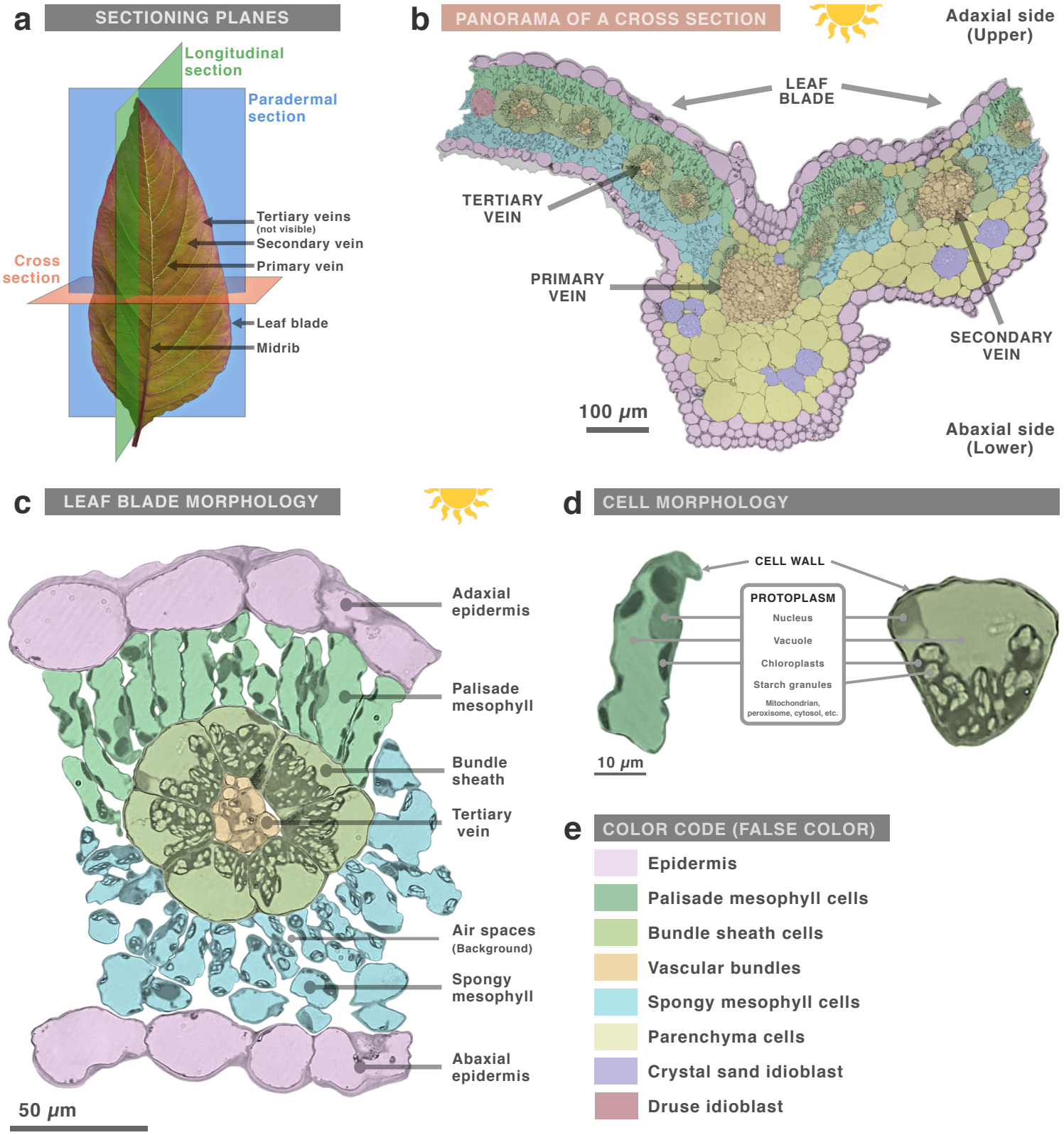

SUPPLEMENTARY FIGURE 1 **Sectional planes of a leaf and panorama of a cross section**

a Anatomy of a leaf and sectioning planes. **b** Light micrograph of a cross-section of a primary vein of an *A. cruentus* leaf. The micrograph was colorized and the background digitally removed. **c** Enlargement of the leaf blade. **d** Enlargement of palisade mesophyll and bundle sheath cells. **e** Color coding (false color) to indicate the different tissues. Plant leaves consist of a blade that is supplied by veins that decrease in diameter as they move away from the midrib. If performed through the midrib, a primary or secondary vein, the cross section can show all leaf tissues as it extends from the adaxial to the abaxial epidermis. Tertiary veins are embedded in the center of the leaf and lack parenchyma associated with vascular bundles, responsible for vein protuberance. Tertiary veins are tightly surrounded by a layer of large bundle sheath cells, and this in turn by a single layer of mesophyll cells, forming a wreath shape called "Kranz anatomy". Mesophyll is divided into palisade (receive direct sunlight) and spongy. The plant cell has a cell wall, and its protoplasm contains a large vacuole and other organelles. Kranz anatomy and differentiated mesophyll tissue (palisade and spongy) are not present in all plant leaves. Kranz anatomy enhances carbon fixation in plants known as C_4, and plants lacking it are known as C_3.

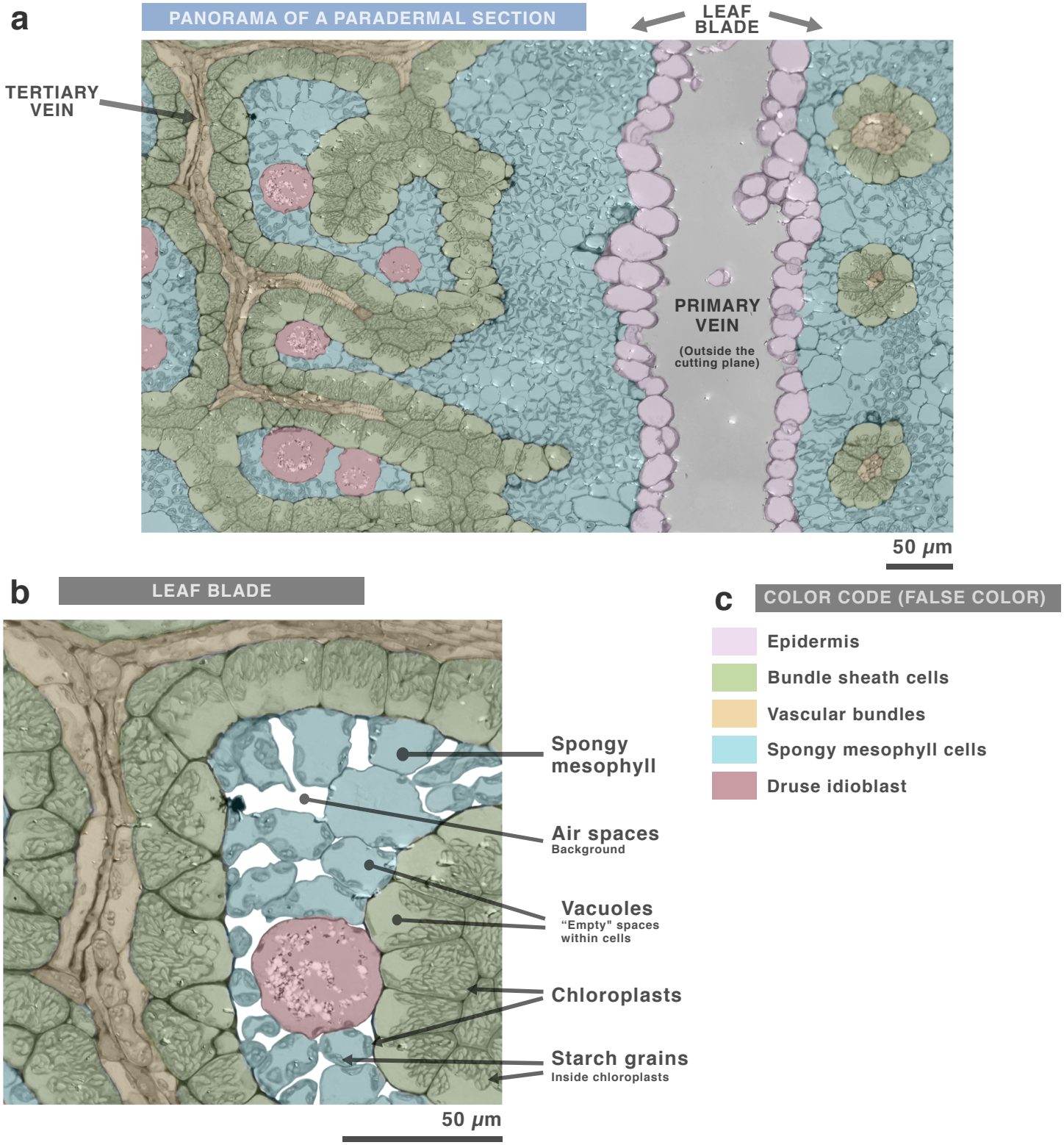

SUPPLEMENTARY FIGURE 2 **Panorama of a paradermal section**

a Light micrograph of a paradermal section of an *A. cruentus* leaf blade. The micrograph was colorized and the background digitally removed. **b** Magnification of a. **c** Color coding (false color) to indicate different tissues. The paradermal section is useful to study the distribution of tertiary veins, a greater number of minority cells such as druse idioblasts, and a greater extent of vascular bundles. Cross section can show all tissues of the leaf, but its extent is limited by the leaf thickness. Paradermal section can show a greater extent of leaf tissues, but the variety is limited. Because the leaf is not flat, the paradermal section usually leaves gaps where the major veins (midrib and primary and secondary veins) used to be. The mid-thickness is the best zone to study because it contains the greatest cellular diversity. A superficial section will show only epidermal cells, a ¾ thickness section will show only mesophyll cells.

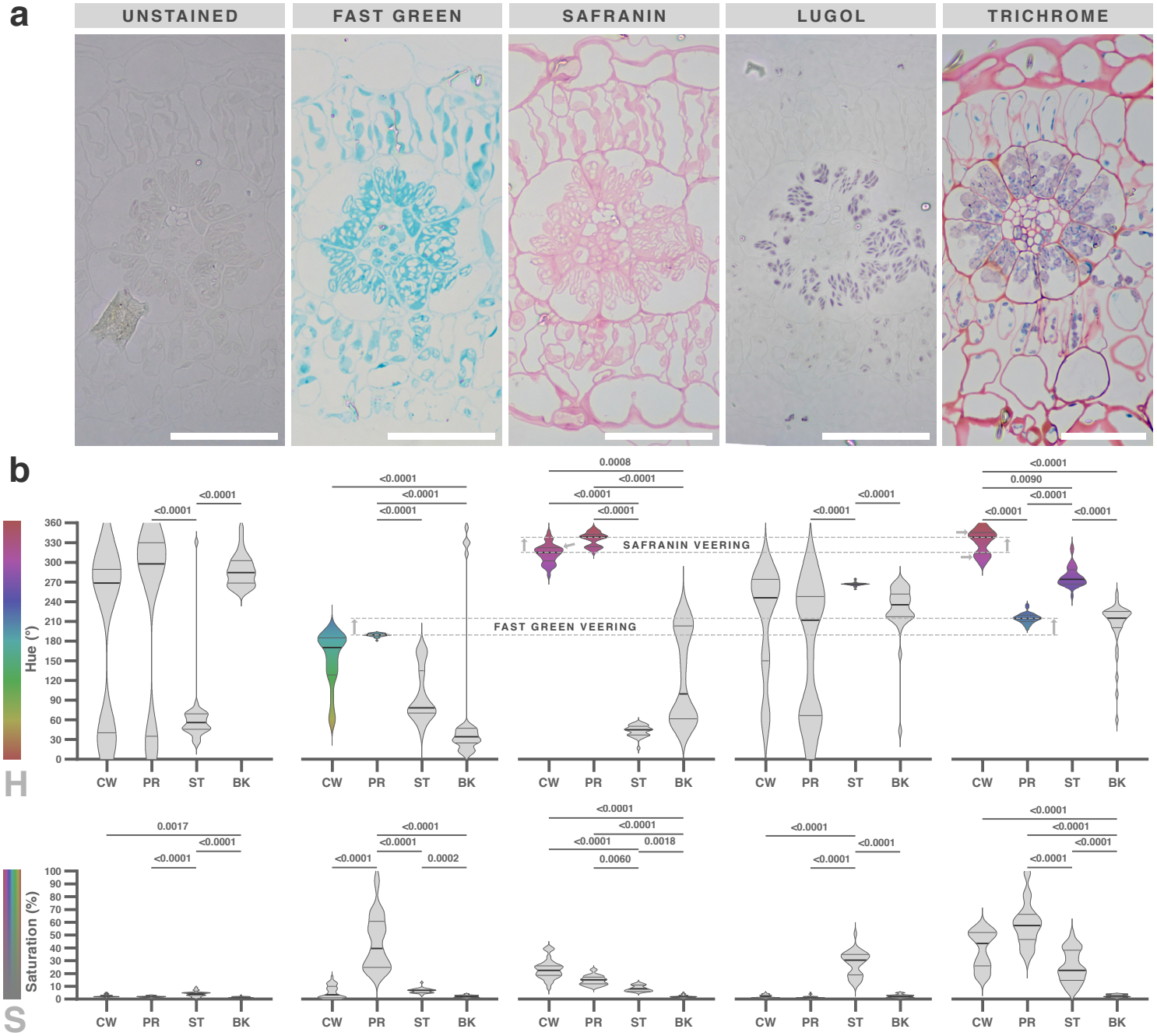

c

		HUE			SATURATION		
		Only	Trichrome	Veering	Only	Trichrome	Difference
Fast green	CW	170			4		
	PR	189	215	**26**	40	58	**18**
Safranin	CW	315	338	**23**	23	44	**21**
	PR	339			15		
Lugol	ST	267	274	**7**	31	23	**-8**

SUPPLEMENTARY FIGURE 3 **Trichrome dyes show different affinities for cellular structures when used alone or in combination**

a Light micrograph of a cross section of *A. cruentus* leaf in resin before staining and after staining with fast green, safranin, lugol, and all three dyes (trichrome). Scale bar = 50 μm. **b** Violin plots (n=30) with median, interquartile range, and color range (filled, only for saturation ≤ 15%) observed in cell wall (CW), protoplasm (PR), starch granules (ST), and background (BK). Kruskal-Wallis ANOVA and Dunn's post-test were performed, differences are shown with $p<0.01$. **c** Changes in medians between only dyes and in trichrome combination. Resin sections are colorless and barely distinguishable. Fast green stained the PR turquoise in a very discrete hue range (181 - 193°) and very broad saturation (19-95%). It also stained CW in a very broad hue range (yellow 60° to 196°), but with very weak saturation (0-17%). Safranin stained both CW and PR in magenta to reddish: PR in hues of 315-353° and saturation of 9-23%, and CW in hues of 280-346° and saturation of 9-40%. Lugol stained mauve only the ST in a discrete hue range (259-275°) and a broad saturation range (11-51%). None of the dyes stained the resin BK and vacuoles. In the trichrome combination the PR remained turquoise, the CW magenta to reddish and the ST mauve. However, there were slight changes in hue (veering) and significant changes in saturation. The CW veered from magenta to red hues, the PR from turquoise to blue hues, and both increased in saturation. Also, the hue range of the ST broadened and lost saturation.

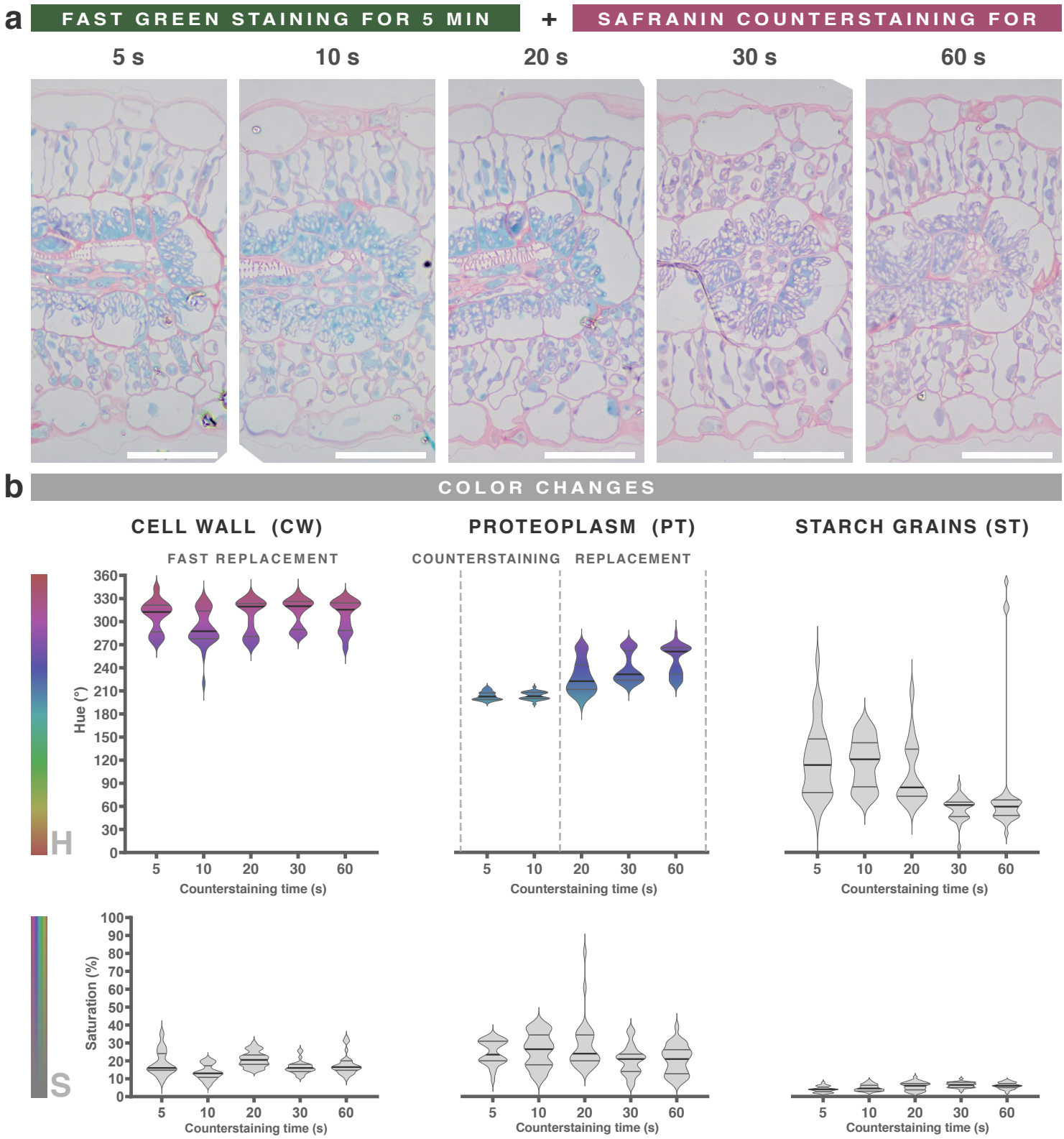

SUPPLEMENTARY FIGURE 4 **Fast green-stained sections can be correctly counterstained with safranin for 5 to 10 s**

a Light micrograph of *A. cruentus* leaf sections stained with fast green for 5 min and counterstained with safranin at different times. Scale bar = 50 μm. **b** Violin plots (n=30) with median, interquartile range and color range observed in cell wall (CW), proteoplasm (PT) and starch granules (ST) at different counterstaining times. Safranin has an affinity for cell wall lignin and suberin, whereas fast green has an affinity for proteoplasm proteins. Safranin rapidly and selectively displaced fast green from the cell wall; its area of affinity (counterstaining). However, after 10 s it began to displace fast green from its affinity area: the proteoplasm (replacement).

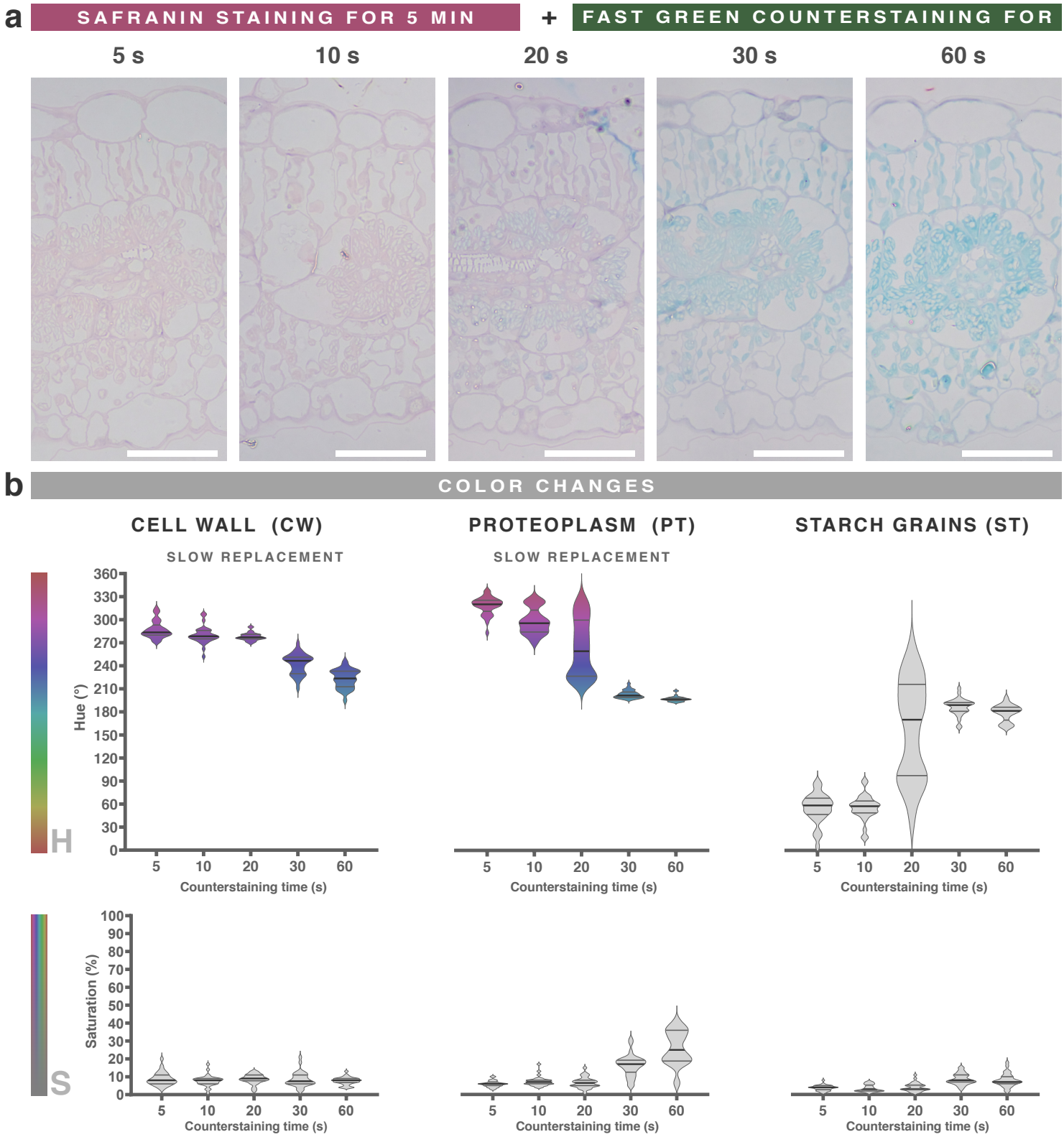

SUPPLEMENTARY FIGURE 5 **Safranin-stained sections cannot be properly counterstained with Fast Green**

a Light micrograph of *A. cruentus* leaf sections stained with safranin for 5 min and counterstained with fast green at different times. Scale bar = 50 μm. **b** Violin plots (n=30) with median, interquartile range, and range of color observed in cell wall (CW), proteoplasm (PT), and starch granules (ST) at different counterstaining times. Safranin has an affinity for cell wall lignin and suberin, whereas fast green has an affinity for proteoplasm proteins. Fast green slowly displaced safranin from the proteoplasm, its affinity area, but in an unsaturated and uneven manner. After 20 s, it also began to displace safranin from the cell wall, producing a poorly saturated result. This order of staining is the original order of Johansen's method. However, only the reverse order gave us good results in resin sections.

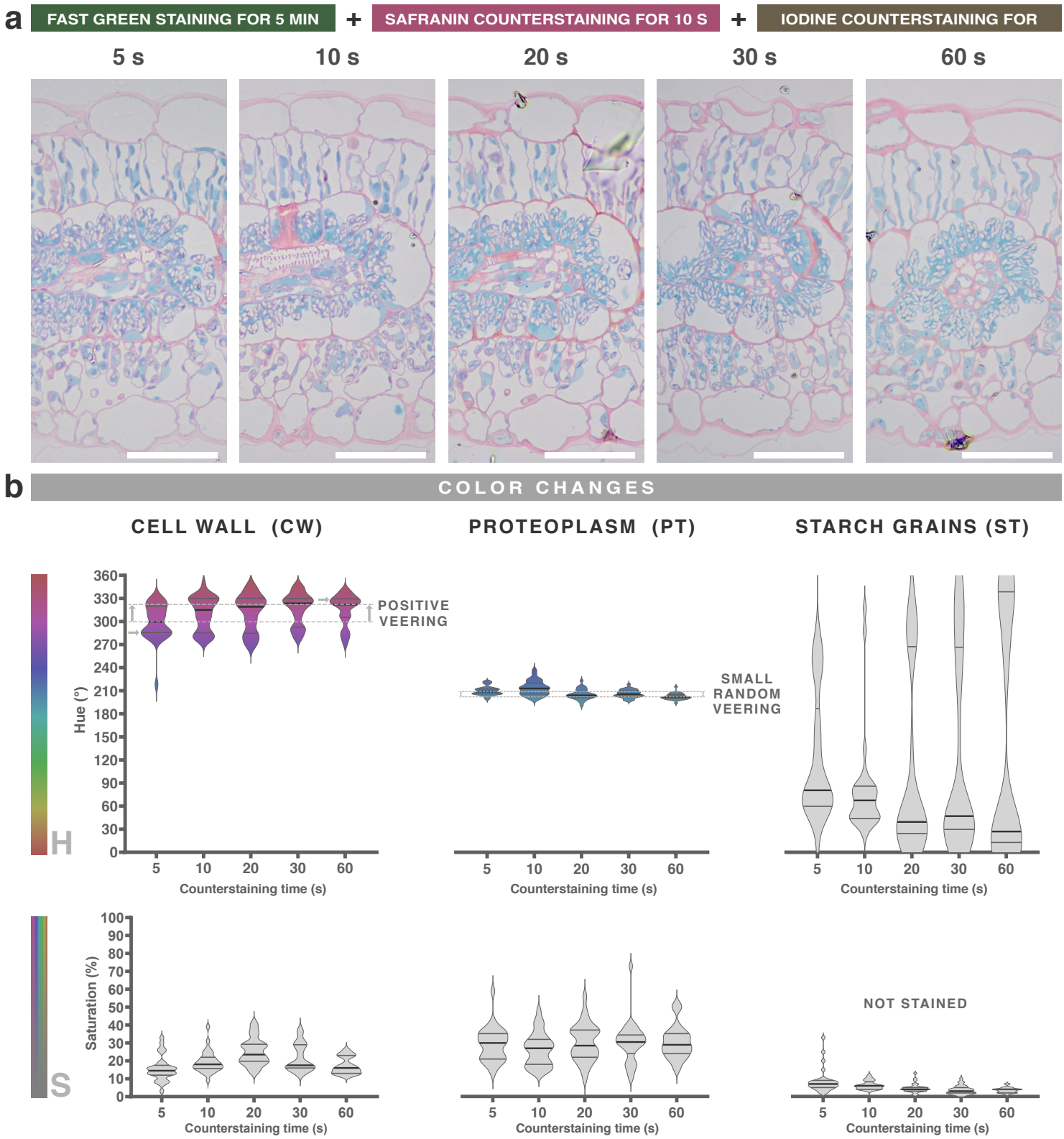

SUPPLEMENTARY FIGURE 6 **Iodine counterstaining produces hue veering in stained sections**

a Light micrograph of *A. cruentus* leaf sections stained with fast green for 5 min, counterstained with safranin for 10 s, and with iodine at different times. Scale bar = 50 μm. **b** Violin plots (n=30) with median, interquartile range, and range of color observed in cell wall (CW), proteoplasm (PT), and starch granules (ST) at different counterstaining times. Iodine has an affinity for starch granules and produces color veering mainly in safranin-stained cell walls. Iodine staining, alone or as a counterstain, produced random intensities of starch granule staining: null, intermediate, or intense. That was independent of time and even between sections of the same sample on the same slide. However, when it occurred, the staining intensity was always homogeneous along the same section. So far, we could not identify the reason for this, and we had to perform many replicates to obtain the desired result. In these sections, the starch granules were not stained. However, a positive time-dependent cell wall veining was observed, as well as a small and random veering in the proteoplasm.

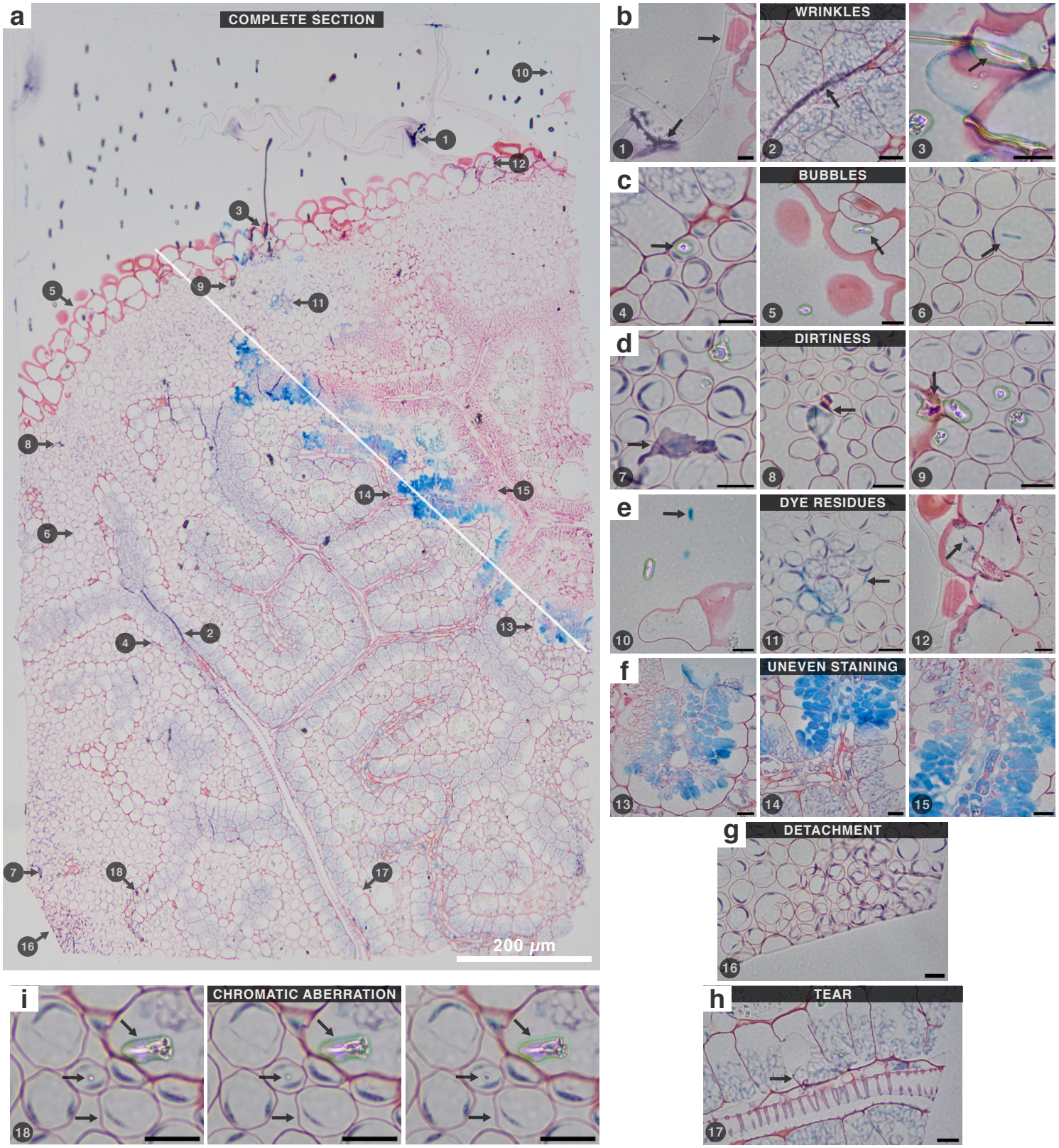

SUPPLEMENTARY FIGURE 7 **Common artifacts on stained resin sections**

a Light micrograph of a paradermal section of an *A. cruentus* leaf. **b-i** Magnification of the artifacts listed in a. **b** Wrinkles are the most common and difficult artifact to avoid; they can cause staining problems and excessive background in immunostaining (**1-3**). **c** Bubbles are small wrinkles that can be recognized by their birefringence (**4,5**). However, they are not always birefringent and can be confused with cellular elements. (**6**). **d** Dirt causes spots, wrinkles and bubbles in the section (**7-9**). Cleanliness is of paramount importance when handling microscopy specimens. **e** Dyes may leave residues on the specimen if not filtered out, or may form precipitates when interacting with other dyes (**10-12**). **f** Inhomogeneous staining is often caused by wrinkles, bubbles, or dirt. However, as with iodine, sometimes there are no clear reasons for its occurrence. In areas **13-15**, there are no wrinkles, bubbles, or dirt, and the section is properly adhered to the glass. However, from there (white line) and upwards, the staining was not homogeneous. **g** Even an area detached from the glass (**16**) was stained homogeneously. **h** Resin sections are prone to tearing, deforming the original histology (**17**). **i** Some artifacts and even the specimen itself may show different colors depending on the focal point (**18**), due to birefringence or chromatic aberration, respectively. Therefore, it is important to define a focusing criterion for all sections.

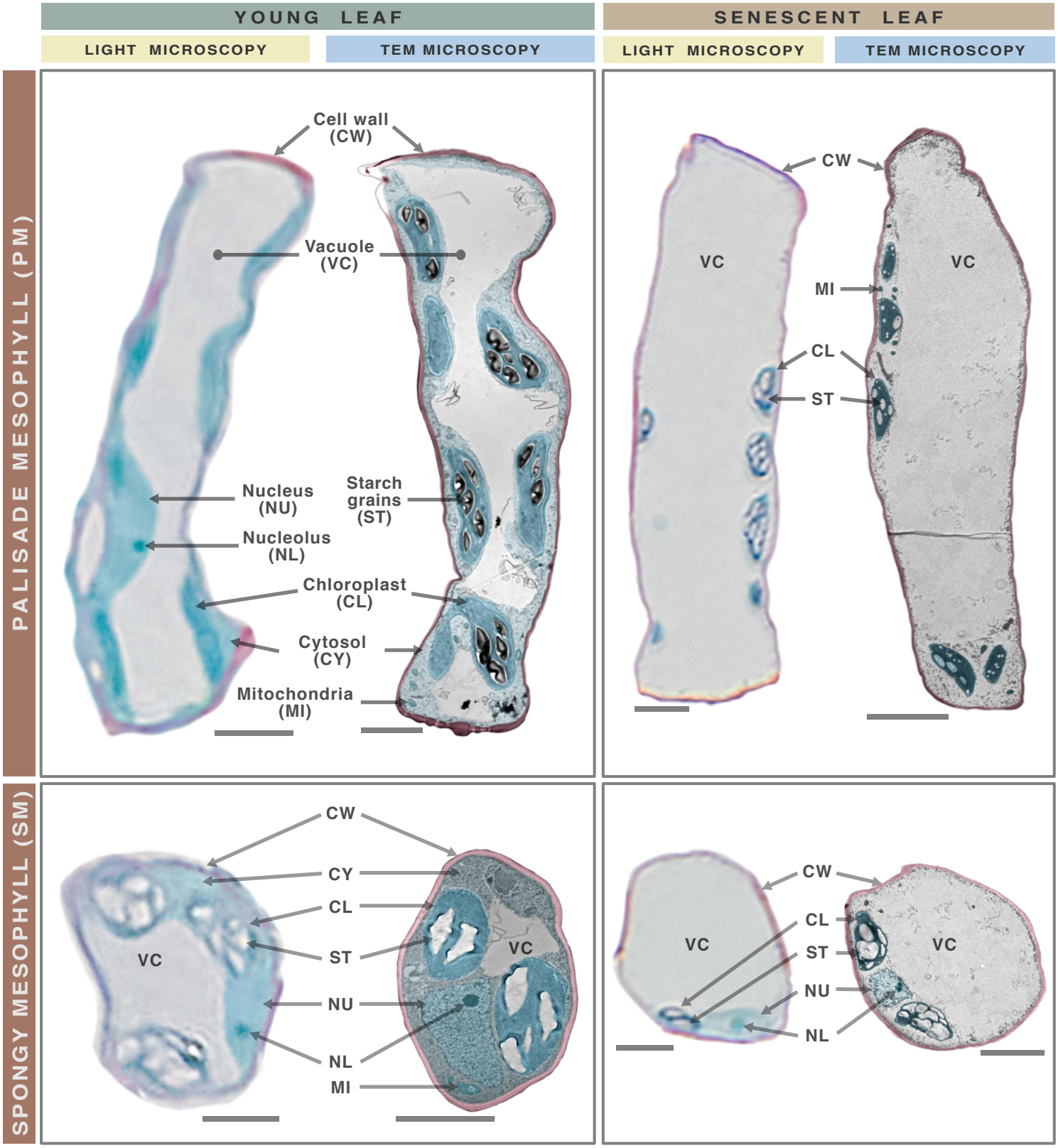

SUPPLEMENTARY FIGURE 8 **Resin-based microtechnique resolution: mesophyll cells**

Palisade and spongy mesophyll cells digitally isolated from light and electron micrographs (not the same cell) of a young (4 weeks old) and a senescent (8 weeks old) *A. cruentus* leaf. Color in light micrograph is from trichrome staining, and in TEM is false color mimicking trichrome staining colors. Scale bar = 5 μm. High-resolution light micrographs revealed several organelles and ultrastructures identified by TEM. The vacuole, identified by its lack of color and texture, covers large areas in the cells. The proteoplasm stained turquoise, but differences in saturation revealed the presence of various organelles identified by TEM. Larger and/or more numerous organelles are usually always present in the micrographs because they are more likely to be in the plane of the section. The opposite is true for small and/or few organelles, such as the nucleus, which are not always observed in the micrographs. The young leaf has a defined cytosol, while the senescent leaf has lost it and its organelles are reduced in size. On the other hand, different amounts of starch granules were observed inside the mesophyll chloroplast.

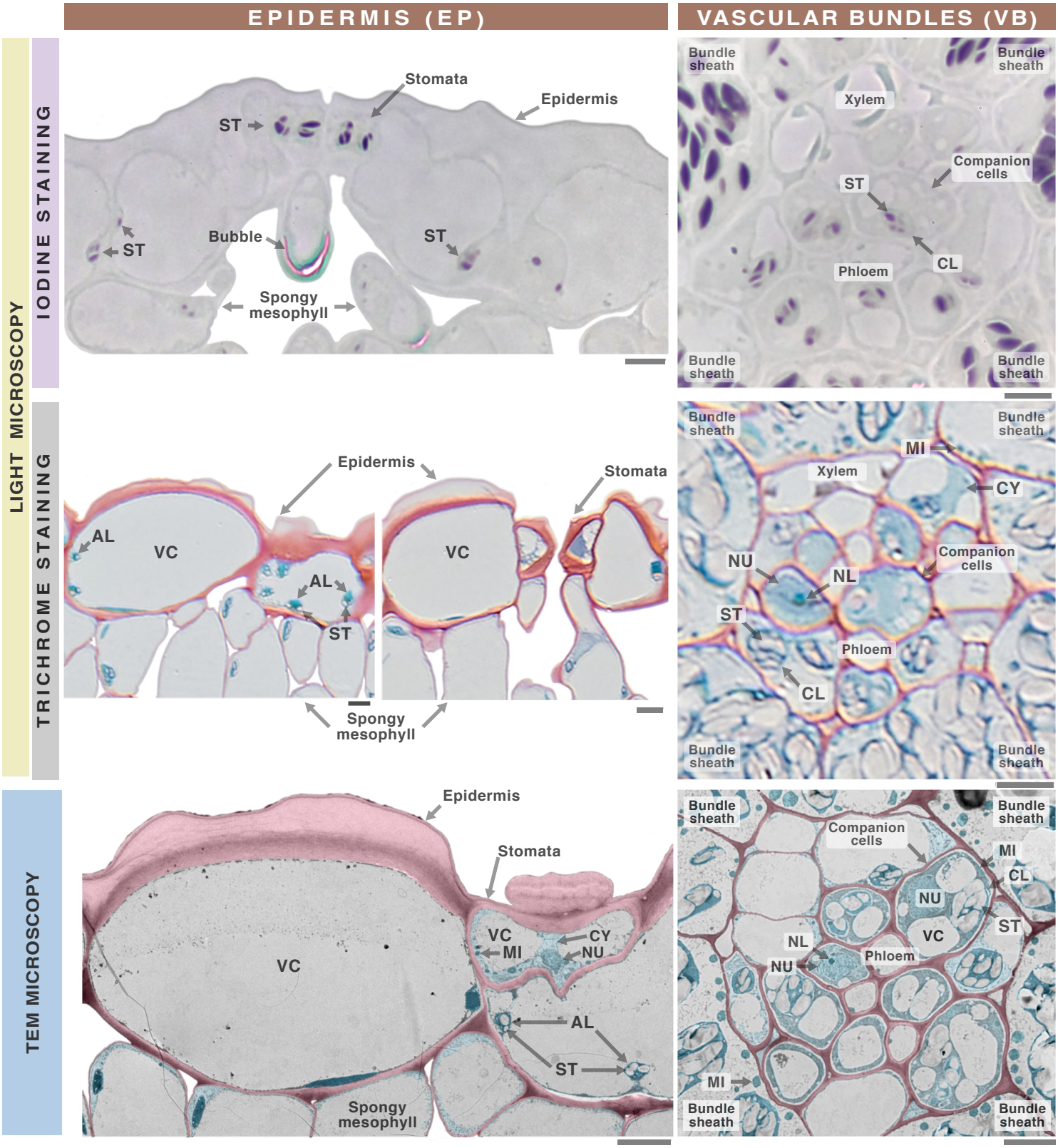

SUPPLEMENTARY FIGURE 9 **Resin-based microtechnique resolution: epidermis and vascular bundle cells**

Epidermis and vascular bundle cells digitally isolated from light and electron micrographs (not the same cell) of a young (4 weeks old) A. cruentus leaf. Color in light micrograph is from trichrome staining, and in TEM is false color mimicking trichrome staining colors. Scale bar = 5 μm. Vacuole (VC), chloroplast (CL), amyloplasts (AL), starch granule (ST), nucleus (NU), nucleolus (NL), cytosol (CY) and mitochondrion (MI). High-resolution light micrographs revealed several organelles and ultrastructures identified by TEM. The epidermis and vascular bundles are formed by different cells. The epidermis consists of epidermal cells, stomata and trichomes. The vascular bundles are formed by the conducting cells xylem and phloem and a variety of accessory cells. The epidermal cells are almost completely devoid of proteoplasm; they mainly retain some traces of amyloplasts with starch granules. Stomata, on the other hand, contain organelle-nourished proteoplasm like a mesophyll cell, as well as significant amounts of starch granules. Xylem and phloem cells are usually observed as hollow and their accessory cells with proteoplasm nourished by organelles, cytosol and starch. Vacuoles and chloroplasts or alternatively amyloplasts are observed in almost all leaf cells.

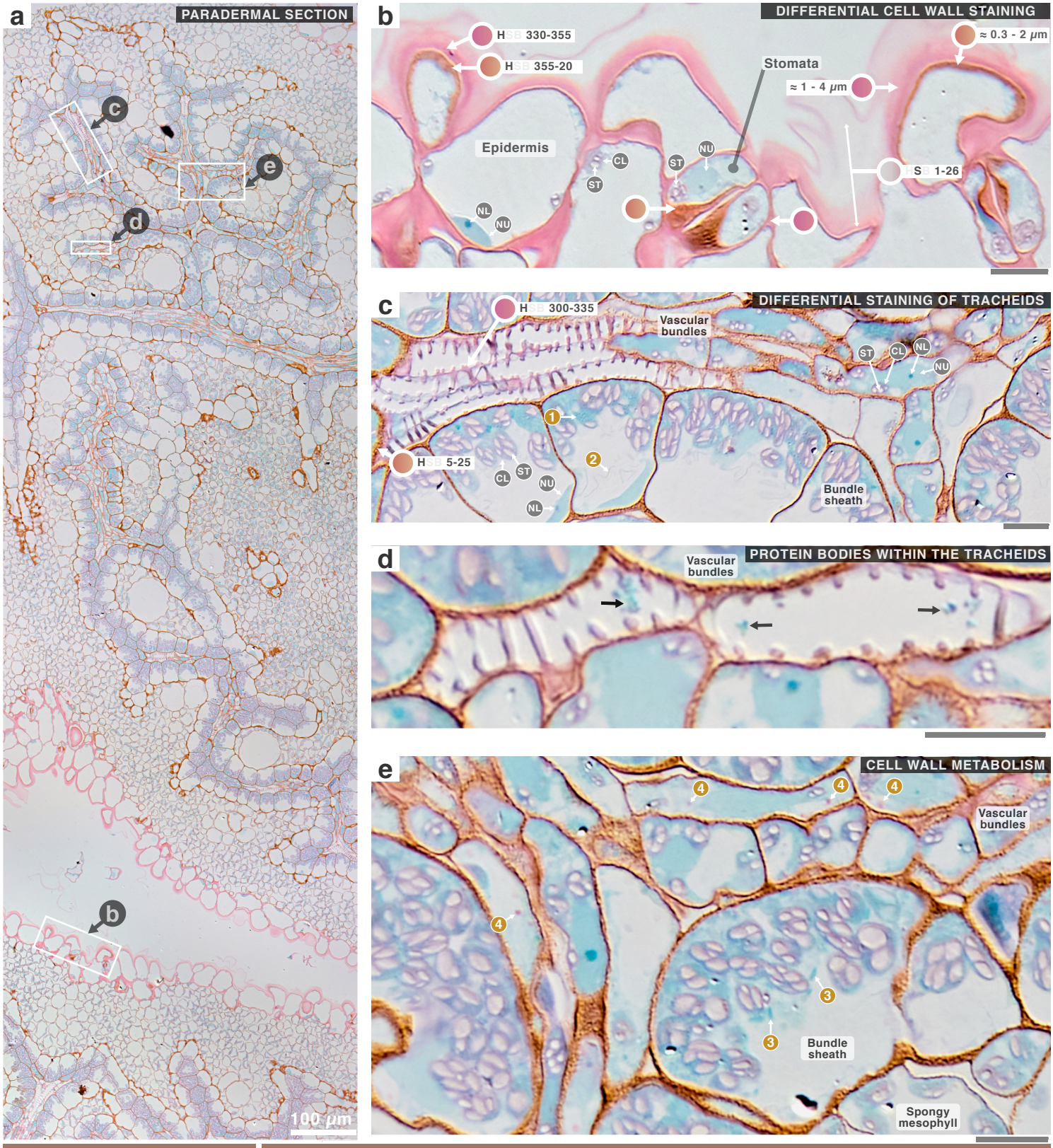

SUPPLEMENTARY FIGURE 10 **Intense iodine counterstaining reveals cell wall composition and ultrastructures**

a Paradermal section of an *A. cruentus* leaf stained with trichrome stain. **b - e** Magnifications of areas marked in a. Scale bars = 10 µm. Vacuole (VC), chloroplast (CL), starch granule (ST), nucleus (NU), nucleolus (NL), and cytosol (CY). a Iodine counterstaining was intense; it stained starch granules, almost all cell walls veered, and ultrastructural details were further contrasted. **b** Epidermal cell walls showed two layers: an internal orange wall and an external magenta wall. Also, the external magenta wall showed a saturation gradient, from inner saturated to outer colorless, ending in a saturated boundary. **c** Almost all cell walls veered to orange, but xylem tracheids remained magenta as the outer layer of the epidermal wall, and some protein bodies were observed inside them (**d**). Various ultrastructural details were observed such as: chloroplasts with granular texture (**1**), membranes inside vacuoles (**2**), rod-shaped organelles (**3**), and vesicular trafficking of cell wall material (**e, 4**).

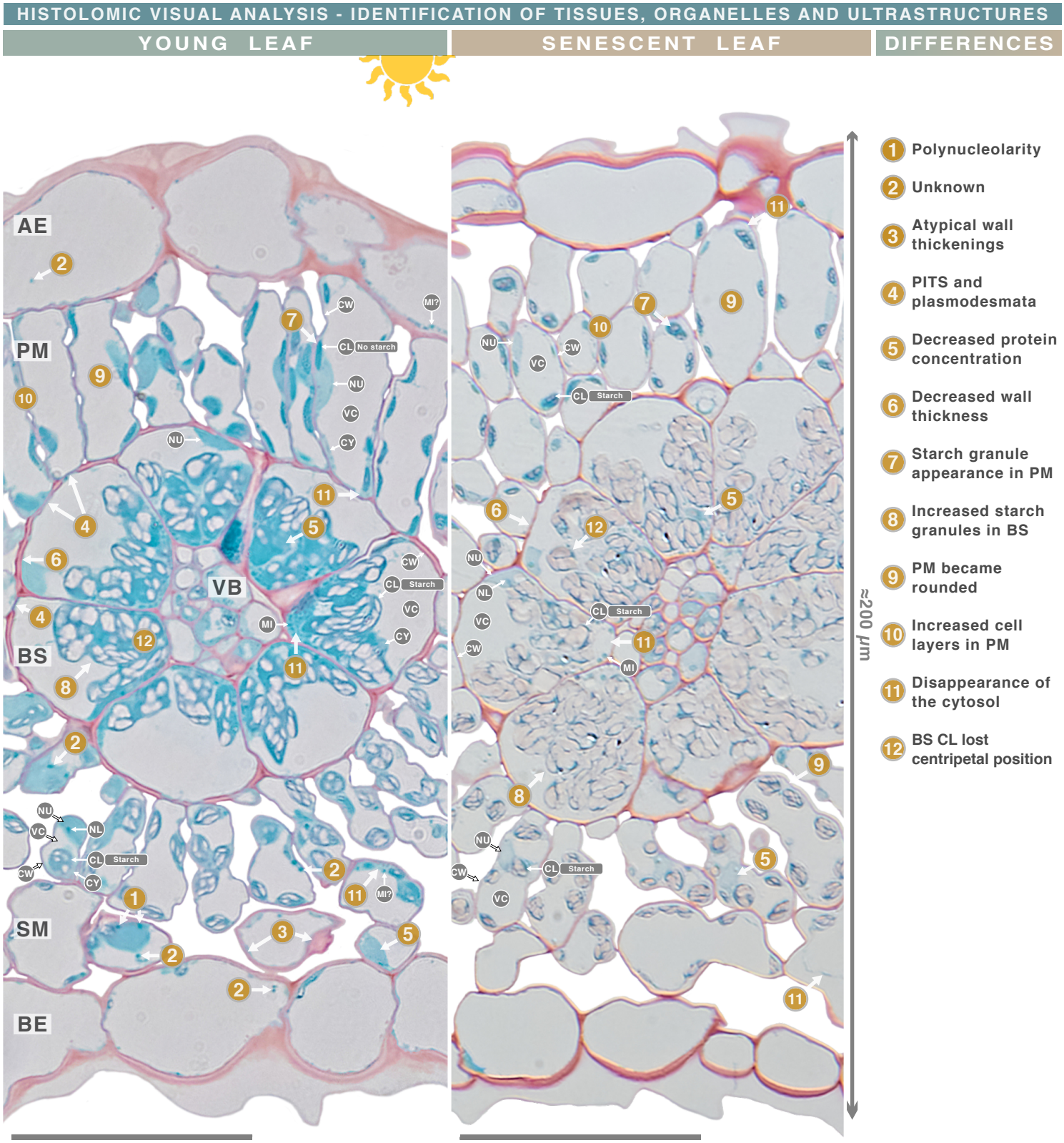

SUPPLEMENTARY FIGURE 11 **Histolomic analysis – Visual analysis**

Light micrographs of cross sections of young (4 weeks) and senescent (8 weeks) leaves of *A. cruentus* stained with trichrome staining. Scale bar = 50 μm. Adaxial epidermis (AE), palisade mesophyll (PM), bundle sheath (BS), vascular bundles (VB), spongy mesophyll (SM) and, abaxial epidermis (BE). Cell wall (CW), vacuole (VC), chloroplast (CL), starch granule (ST), nucleus (NU), nucleolus (NL), cytosol (CY) and mitochondrion (MI). Visual analysis is the first step in histolomic analysis, the main aim of which is to identify tissues, general morphology, organelles and some ultrastructural details. It helps to define the boundaries for micrograph segmentation, relevant features for data analysis, as well as unique traits to highlight. The *A. cruentus* leaf has an average thickness of about 200 μm and 8 to 10 cells (not including VB), a clear kranz anatomy and a clear differentiation between PM and SM. BS, VB, PM and SM are well nourished with organelles, mainly chloroplasts, while the epidermis barely has proteoplasm. Several ultrastructural details were observed: Some nuclei with apparent polynucleolarity (**1**), unknown proteinaceous structures (perhaps mitochondrion) with atypical size and/or location (**2**), atypical wall thickenings in SM (**3**) and PITS-plasmodesmata between PM and BS (**4**). Also, compared to the young leaf, the senescent leaf had reduced protein concentration (**5**), reduced cell wall thickness (**6**), increased ST in PM (**7**) and BS (**8**), PM became rounded (**9**) and had more cell layers (**10**), the cytosol diapered (**11**) and the CL of BS lost its centripetal position (**12**).

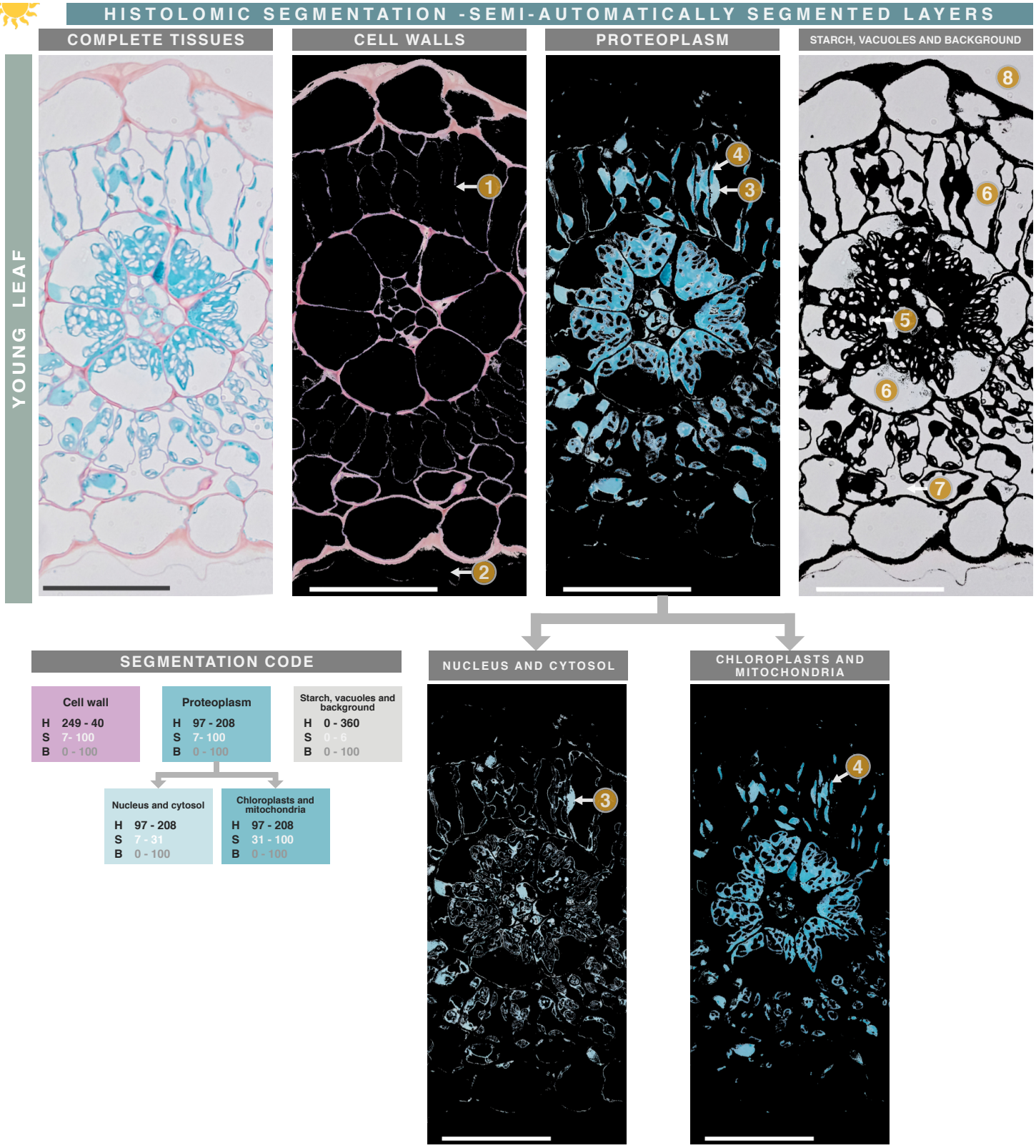

SUPPLEMENTARY FIGURE 12 **Histolomic analysis – Semi-automated segmentation**

Light micrograph of a trichrome-stained cross section of a young amaranth leaf and the layers obtained after color-based segmentation of its tissue components. Scale bar = 50 μm. The micrograph was digitally segmented in MatLab using the “color threshold” app and the "segmentation code" settings to isolate the stained and unstained tissue components. Thin and lightly stained mesophyll cell walls lacked continuity (**1**), as did the outer epidermal walls (**2**). Differences in saturation of the proteoplasm allowed visual identification of organelles and cytosol, as well as secondary segmentation into low-saturated proteoplasm (**3**), such as cytosol and nucleus, and high-saturated proteoplasm, such as chloroplasts and mitochondria (**4**). Iodine counterstaining was null in the starch granules of this section (**5**), so they were segmented along with other unstained components such as vacuoles (**6**), intercellular air spaces (**7**), and resin background (**8**). Semi-automatic segmentation is convenient, but fails in thin and poorly stained cell walls, and also requires further manual segmentation to sub-segment the layers per tissue.

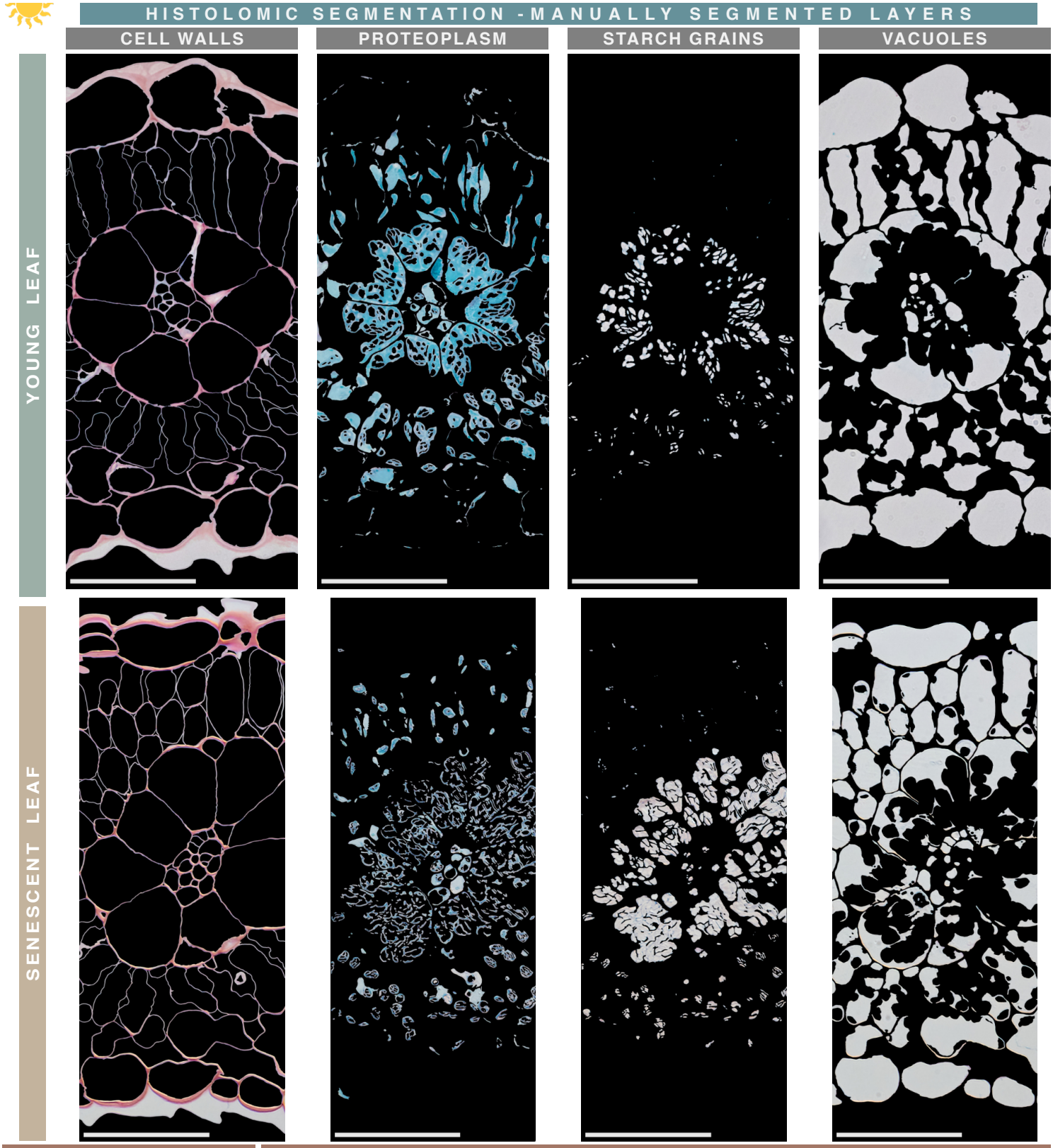

SUPPLEMENTARY FIGURE 13 **Histolomic analysis - Manual segmentation of tissue components of an entire section**

Manually segmented layers form light micrographs of a trichrome-stained cross section of a young and senescent amaranth leaf. Scale bar = 50 μm. Manual segmentation is time-consuming, but necessary to delineate thin and/or poorly stained cell walls that are lost in semi-automated segmentation. Each layer is more than just an attractive image; it contains size, perimeter, area and shape information that can be analyzed for morphometric measurements, as well as color intensity by area (densitometry) information that can be analyzed for compositional measurements. Clear and continuous cell boundaries are important for further morphometric measurements. In addition, manual segmentation is necessary to separate layers per tissue for independent study.

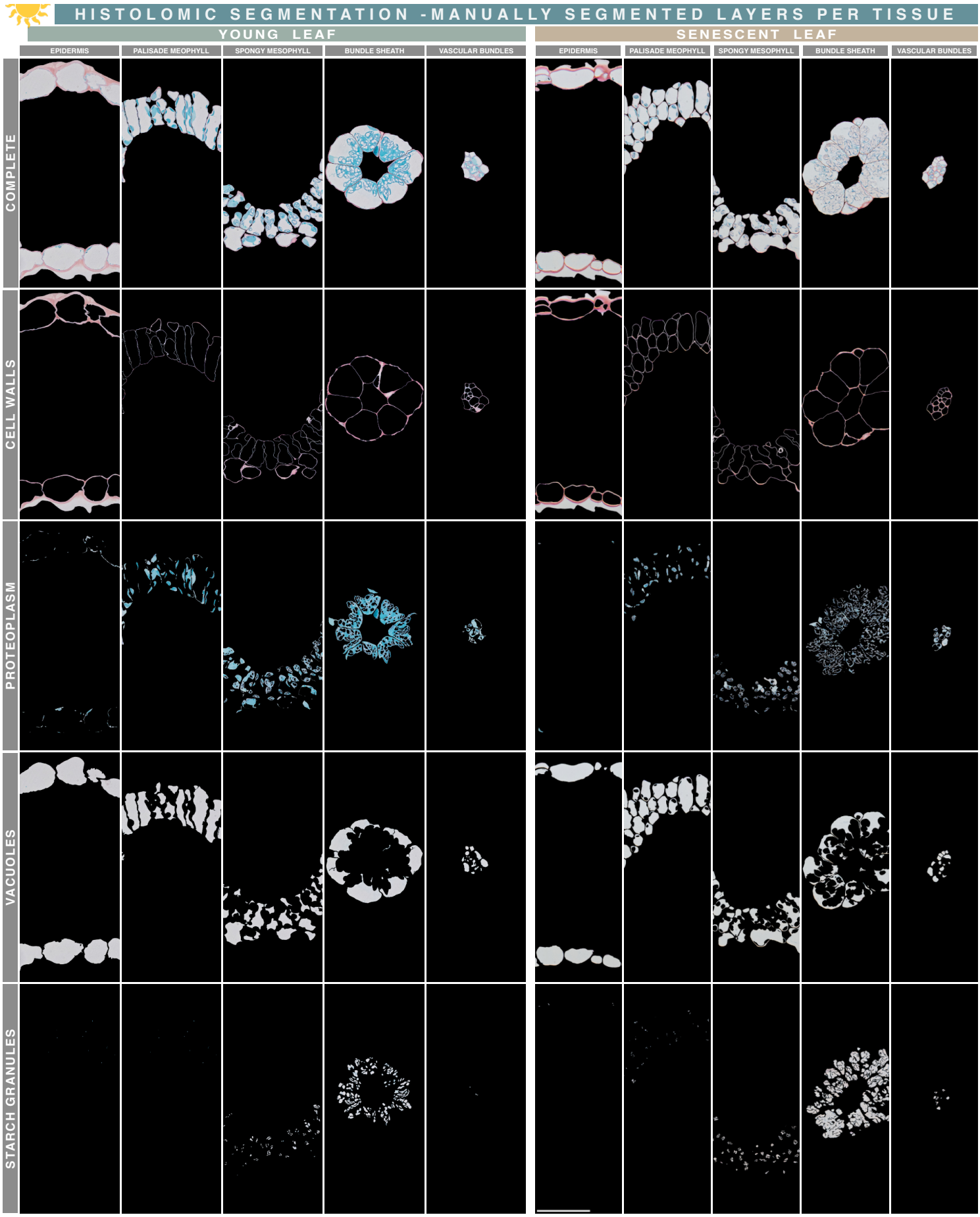

SUPPLEMENTARY FIGURE 14 **Histolomic analysis - Manual segmentation of tissue components per tissue**

Manually segmented layers form light micrographs of a trichrome-stained cross section of a young and senescent amaranth leaf. Scale bar = 50 μm. Histolomics aims at the individualized phenotypic study of the tissues of an organ. We visualize cell-by-cell segmentation and analysis as the future of histolomics, which is currently very laborious to perform manually.

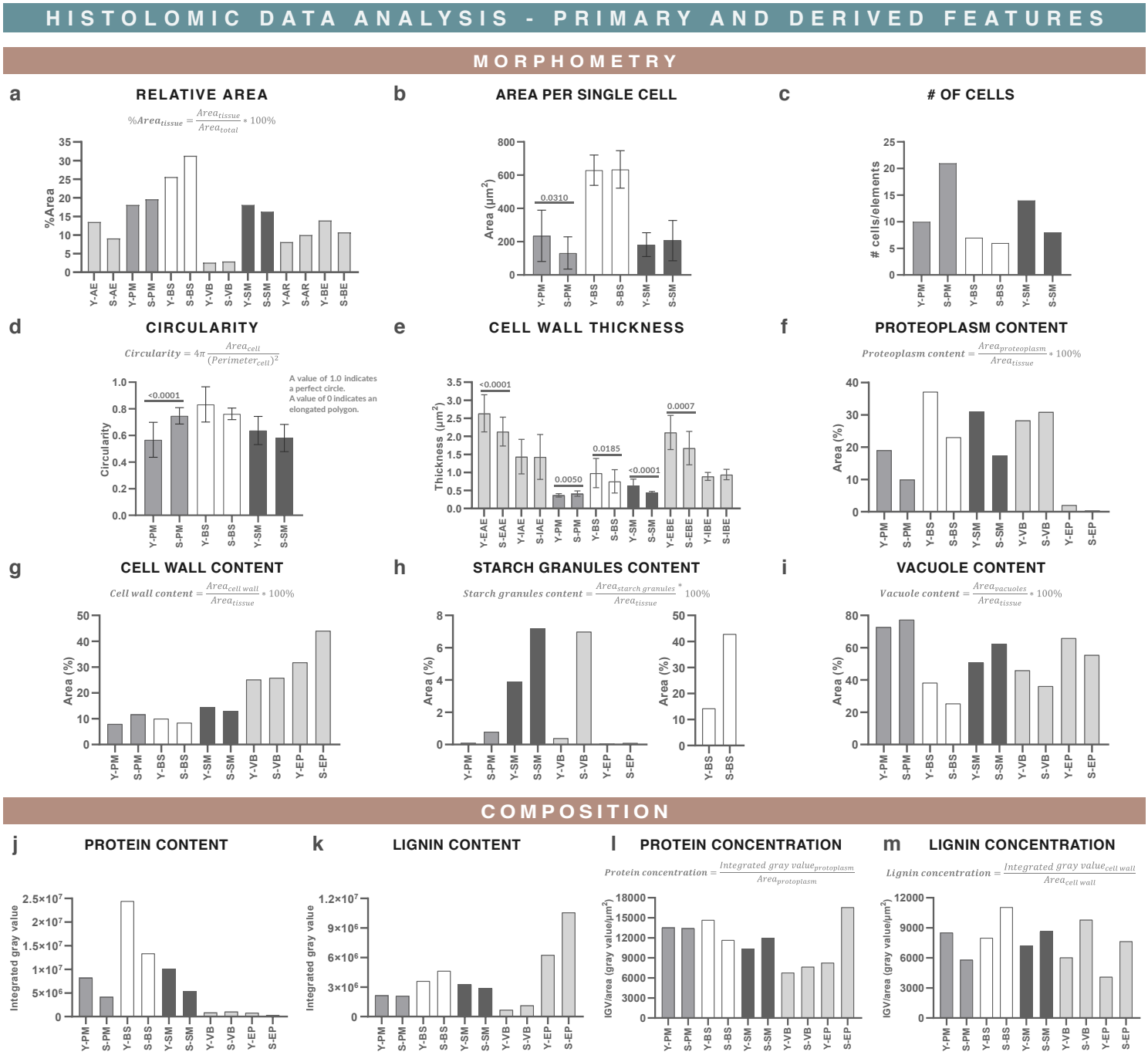

SUPPLEMENTARY FIGURE 15 **Histolomic analysis – Data analysis**

Morphometric and compositional analysis of a trichrome-stained cross section of a young and senescent amaranth leaf. Adaxial epidermis (AE), abaxial epidermis (BE), adaxial inner epidermis (IAE), adaxial outer epidermis (EAE), abaxial inner epidermis (IBE), abaxial outer epidermis (EBE), palisade mesophyll (PM), spongy mesophyll (SM), bundle sheath (BS), vascular bundles (VB), air spaces (AR), young leaf (Y), and senescent leaf (S). For measurements with replicates, a t-test was performed comparing young vs. senescent leaf, differences are shown with $p<0.05$. Histolomics needs its own features and formulas for in-depth study of morphometric and compositional traits beyond the naked eye. We propose three types of histolomic features: primary, derived, and composite. Primary features are individual measurements on the layers, such as cell count, thickness, areas, perimeters and total protein/lignin content. Derived features are ratios or combinations of two or more primary features, such as protein/lignin concentrations and organelles content. Composite features are combinations of different derived and primary features, can be weighted and are useful for quantitative comparison of complex tissue behavior (Supplementary Fig. 24). In this figure, we present primary and derived features and their formula (when apply). Their values gave a quantitative view of the differences observed in the visual analysis of the senescent leaf with respect to the young leaf: decreased protein concentration (**l**), decreased cell wall thickness (**e**), more starch granules in the PM (**h**), the PM became rounded (**d**), and increased layers of the PM (**c**). Other important features related to kranz anatomy were observed between BS, PM and SM. BS was by far the largest tissue area (**a**), had larger cells (**b**), had less vacuole content (**i**), and had the largest content of proteoplasm (**f**), protein (**j**), and starch granules (**h**). The bundle sheath also had slightly higher lignin concentration (m) and had thicker cell walls (**g**, **e**). Protein and lignin measurements are semi-quantitative as they are not related to a calibration curve (**j-m**). However, in comparative studies, the differences between quantities are usually more relevant than the absolute value itself.

SEMI-AUTOMATICALLY SEGMENTED LAYERS OF AN INTENSELY IODINE COUNTERSTAINED TISSUE

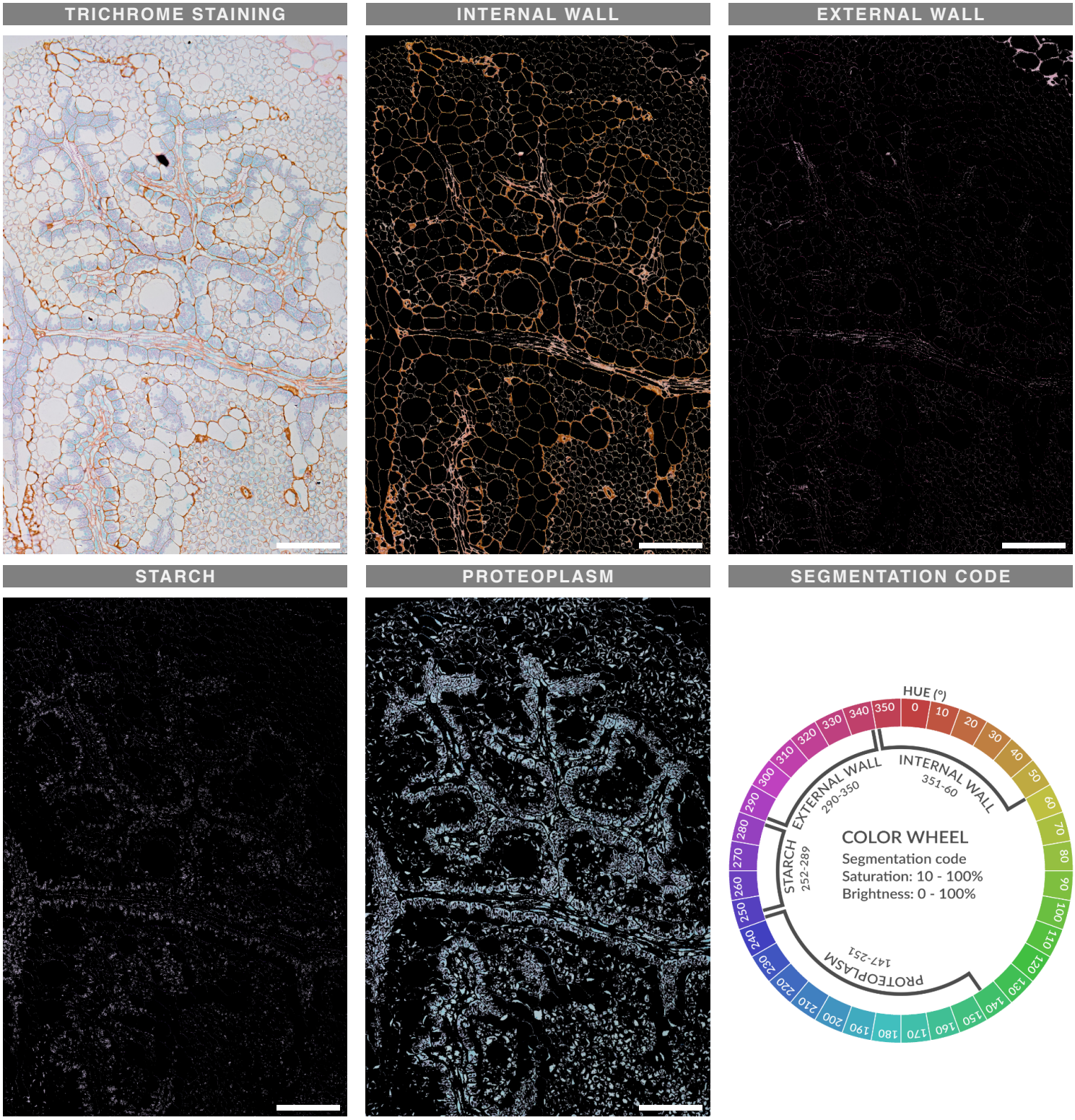

SUPPLEMENTARY FIGURE 16 **Intense iodine counterstaining allows further color (composition) segmentation**

Semi-automatic color segmentation of a paradermal section of an *A. cruentus* leaf stained with trichrome staining. Scale bar = 100 μm. The color wheel conveniently shows the hue range assigned to each tissue component, as well as the saturation and brightness settings for segmentation. Intense iodine counterstaining veered almost all cell walls to orange, except for epidermal walls, which had an internal orange wall and an external magenta wall. The inner wall showed a wide range of reddish, orange, and yellow hues, while the outer wall showed magenta to reddish hues. Color segmentation showed that although the majority of the walls veered toward orange, they also retained some magenta hues. This suggests the presence of two layers of different composition on the cell wall. On the other hand, intense iodine counterstaining allowed segmentation of starch granules and did not produce significant veering in the hue range of proteoplasm as occurred with cell walls. However, the color range of starch granules slightly overlapped with the color range of the outer wall, making the starch granules and outer wall layers "impure". Nevertheless, intense iodine counterstaining differentiated the cell wall color and improved the staining of the thin mesophyll cell walls, thus extending the molecular composition information and improving boundary detection.

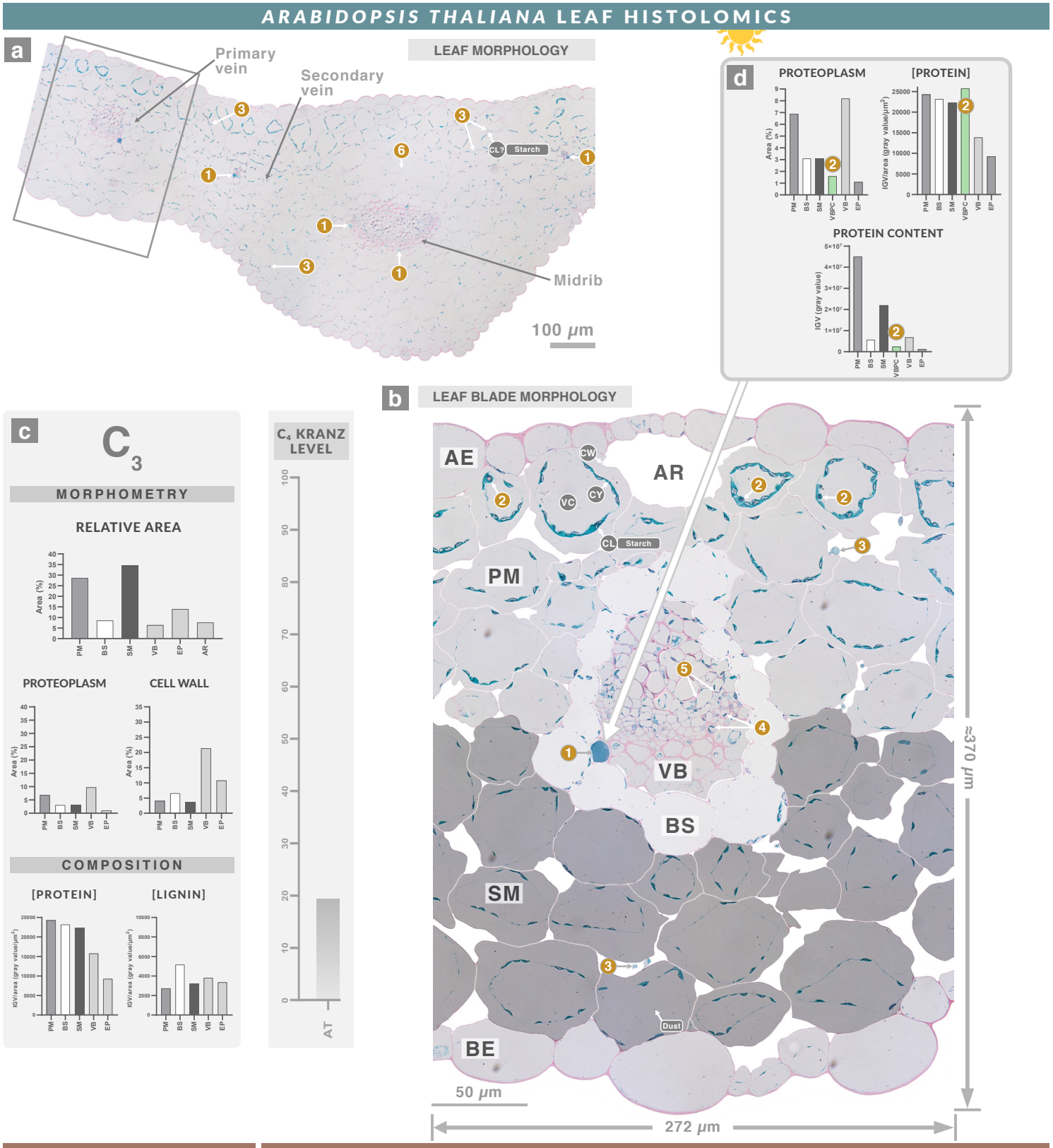

SUPPLEMENTARY FIGURE 17 **Histolome of *Arabidopsis thaliana* leaf**

a Cross section of a trichrome-stained *Arabidopsis thaliana* leaf. **b** Magnification of the squared area in a. **c** Derived (morphometry and composition) and composite (C_4 Kranz level) features of the tissue (same scales for all plant species). **d** Derived features of the vascular bundle proteinaceous cell (VBPC). Adaxial epidermis (AE), abaxial epidermis (BE), palisade mesophyll (PM), spongy mesophyll (SM), bundle sheath (BS), vascular bundles (VB), air spaces (AR). Cell wall (CW), vacuole (VC), chloroplast (CL), starch granule (ST), nucleus (NU), nucleolus (NL), cytosol (CY) and mitochondrion (MI). Although not all plants have a developed BS or differentiated PM and SM, we have highlighted these tissues for comparison purposes. We have increased the brightness of the BS and decreased the brightness of the SM to distinguish them from the other tissues. The leaf of *A. thaliana* had a small BS tightly surrounded by two layers of PM and three layers of SM: not wreath-shaped. Also, all their cells had low proteoplasmic content (c), except for a unique VBPC in the VB with a smooth and well-nourished proteoplasm, covering almost the entire cell cytoplasm (**1**). One VBPC was detected in the VB of the primary vein and two in the secondary vein and midrib, but with less proteoplasm and protein concentration than in the primary vein (a). VBPC had up to 26% of the protein content of the VB in the primary vein (d). On the other hand, some unknown ultrastructural details were observed: organelles with purple dots (**2**), extracellular proteoplasm (**3**), dark purple and rod-shaped organelles in VB (**4**), intermittent coloring in VB cell walls (**5**) and apparently broken cells (**6**).

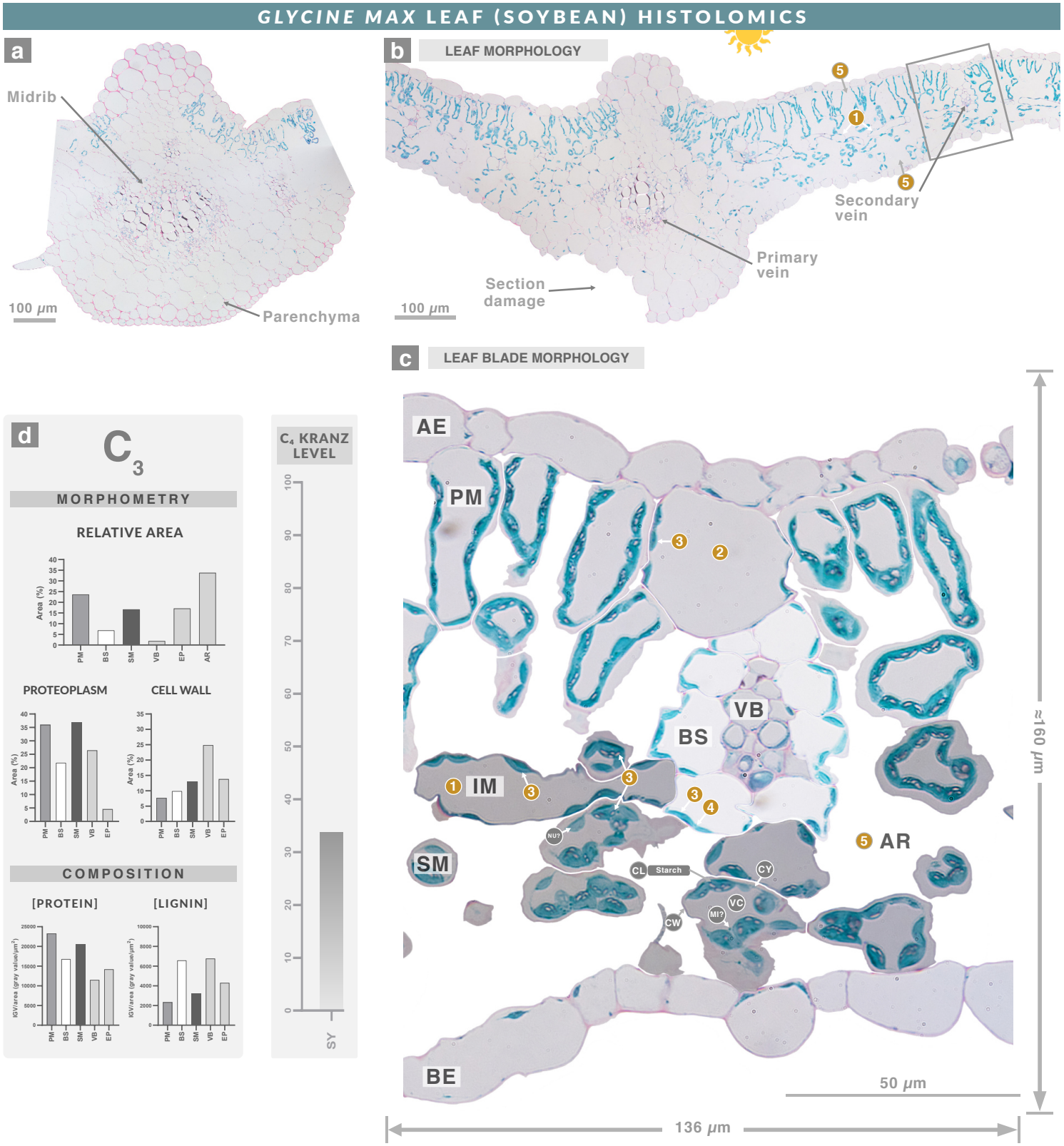

SUPPLEMENTARY FIGURE 18 **Histolome of *Glycine max* leaf**

Cross section of a trichrome-stained *Glycine max* leaf midrib (**a**) and leaf blade (**b**). **c** Magnification of the squared area in b. **d** Derived (morphometry and composition) and composite (C_4 Kranz level) features of the tissue (same scales for all plant species). The leaf of *G. max* had a small BS loosely surrounded by a layer of PM and two layers of SM: not wreath-shaped. We also observed a rod-like mesophyll similar to PM but perpendicular to it, which we called intermediate mesophyll (IM, **1**). Intermediate mesophyll was observed along the blade as well as other rounded PM cells (**2**). Intermediate mesophyll was also compositionally different, as it did not accumulate starch granules like BS and (**2**), and unlike PM and SM (**3**). In addition, despite being a C_3 plant, BS had centrifugally oriented CL; a C_4 characteristic (**4**). Finally, the most prominent morphological feature was the large number of intercellular air spaces (**5**).

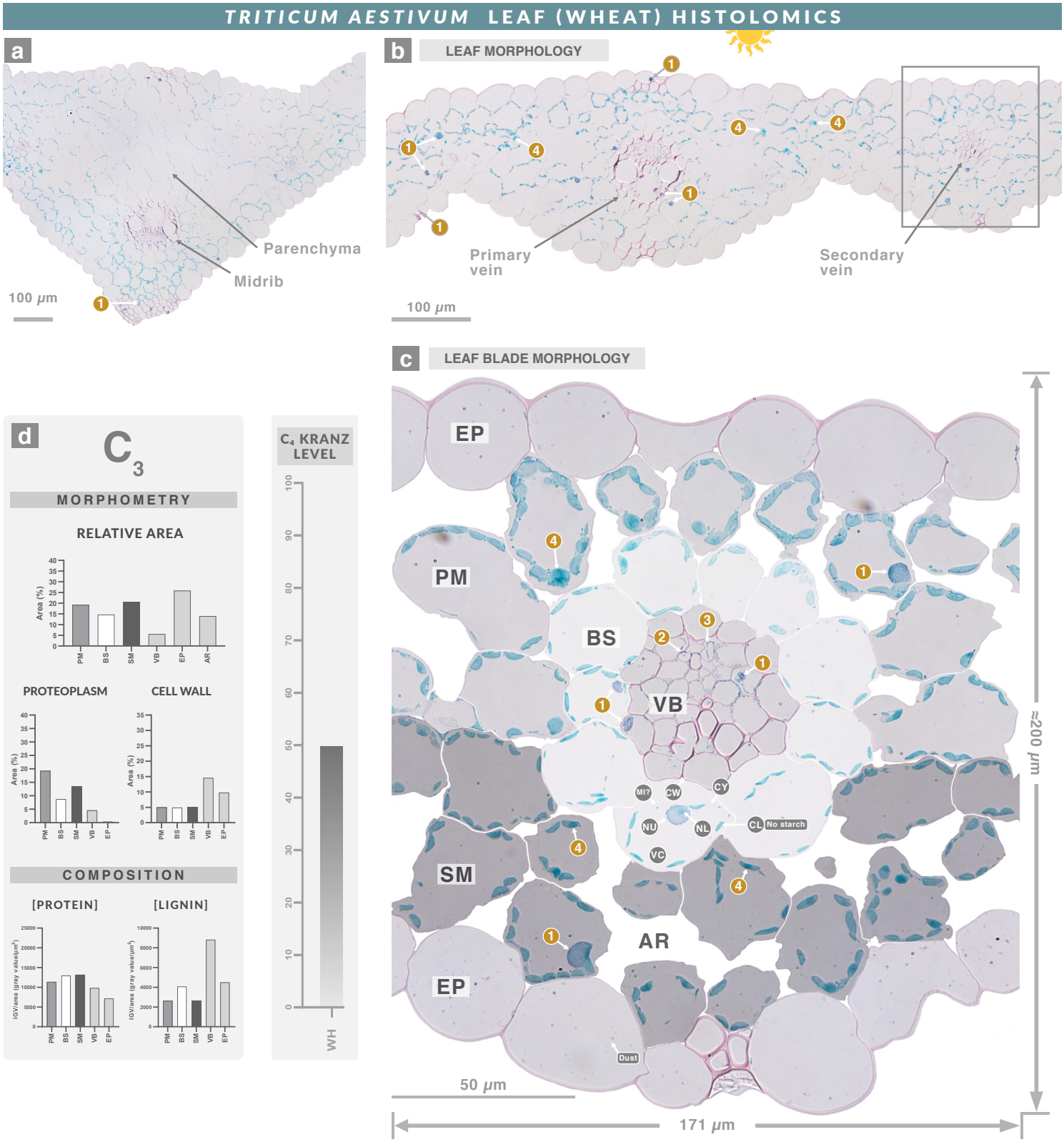

SUPPLEMENTARY FIGURE 19 **Histolome of *Triticum aestivum* leaf**

Cross section of a trichrome-stained *T. aestivum* leaf midrib (**a**) and leaf blade (**b**). **c** Magnification of the squared area in b. **d** Derived (morphometry and composition) and composite (C_4 Kranz level) features of the tissue (same scales for all plant species). The leaf of *T. aestivum* had a large BS tightly surrounded by a layer of undifferentiated PM and two layers of SM: wreath-shaped. Other unique features were observed as: magenta-stained granules in turquoise-stained nuclei (**1**), intermittent magenta-purple staining in VB walls (**2**), VB barely had proteoplasm (**3**), and the protein content of some organelles was polarized (**4**).

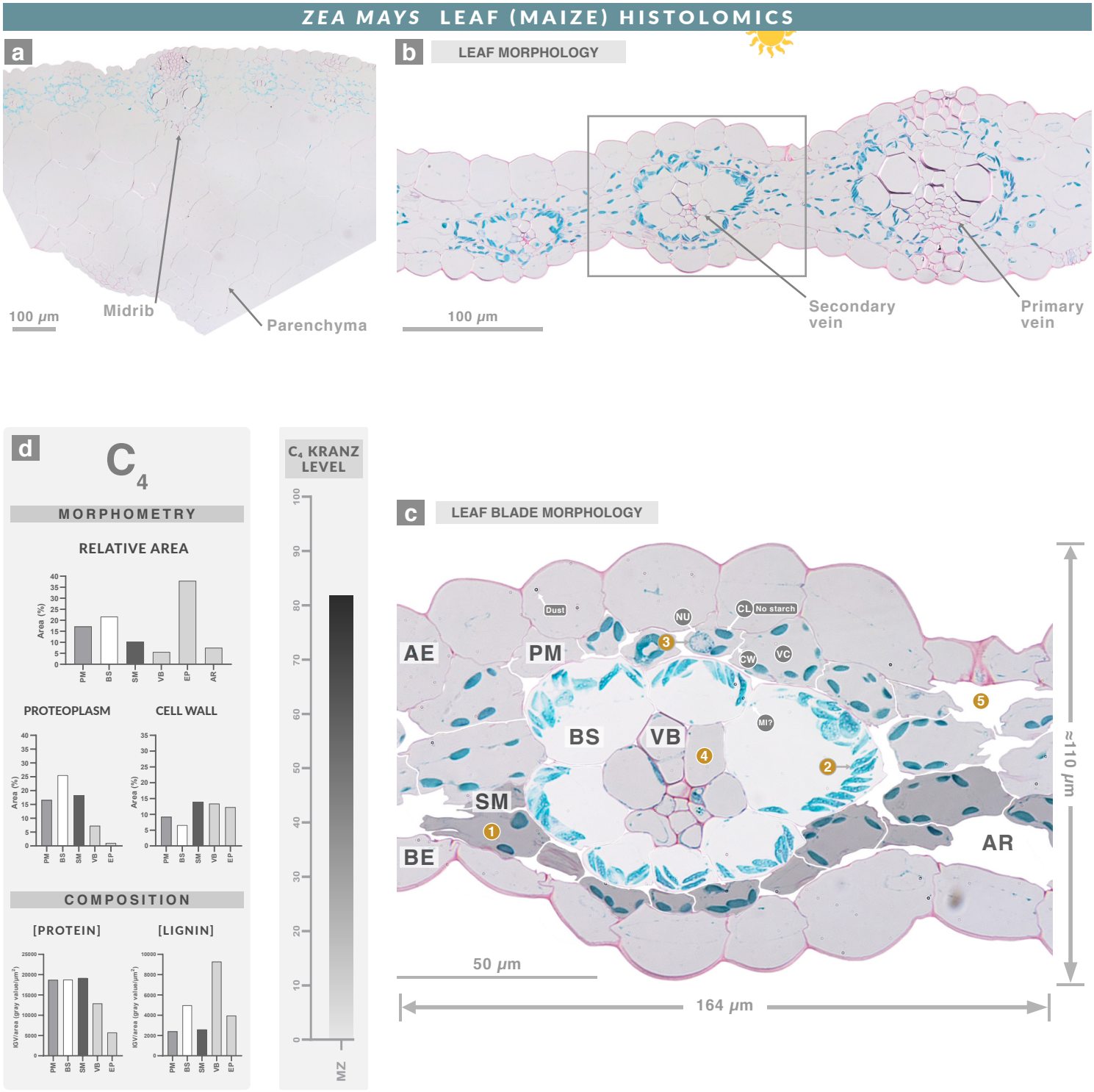

SUPPLEMENTARY FIGURE 20 **Histolome of *Zea mays* leaf**

Cross section of a trichrome-stained *Z. mays* leaf midrib (**a**) and leaf blade (**b**). **c** Magnification of the squared area in b. **d** Derived (morphometry and composition) and composite (C_4 Kranz level) features of the tissue (same scales for all plant species). The leaf of *Z. mays* had a very large BS tightly surrounded by a layer of undifferentiated PM and a layer of SM: wreath-shaped. SM between VB had an elongated shape with sharp edges (**1**), and BS chloroplasts had a centripetal position (**2**). On the other hand, nuclei had granules (**3**), VB had little proteoplasm **(4**), and there were very few intercellular air spaces (**5**).

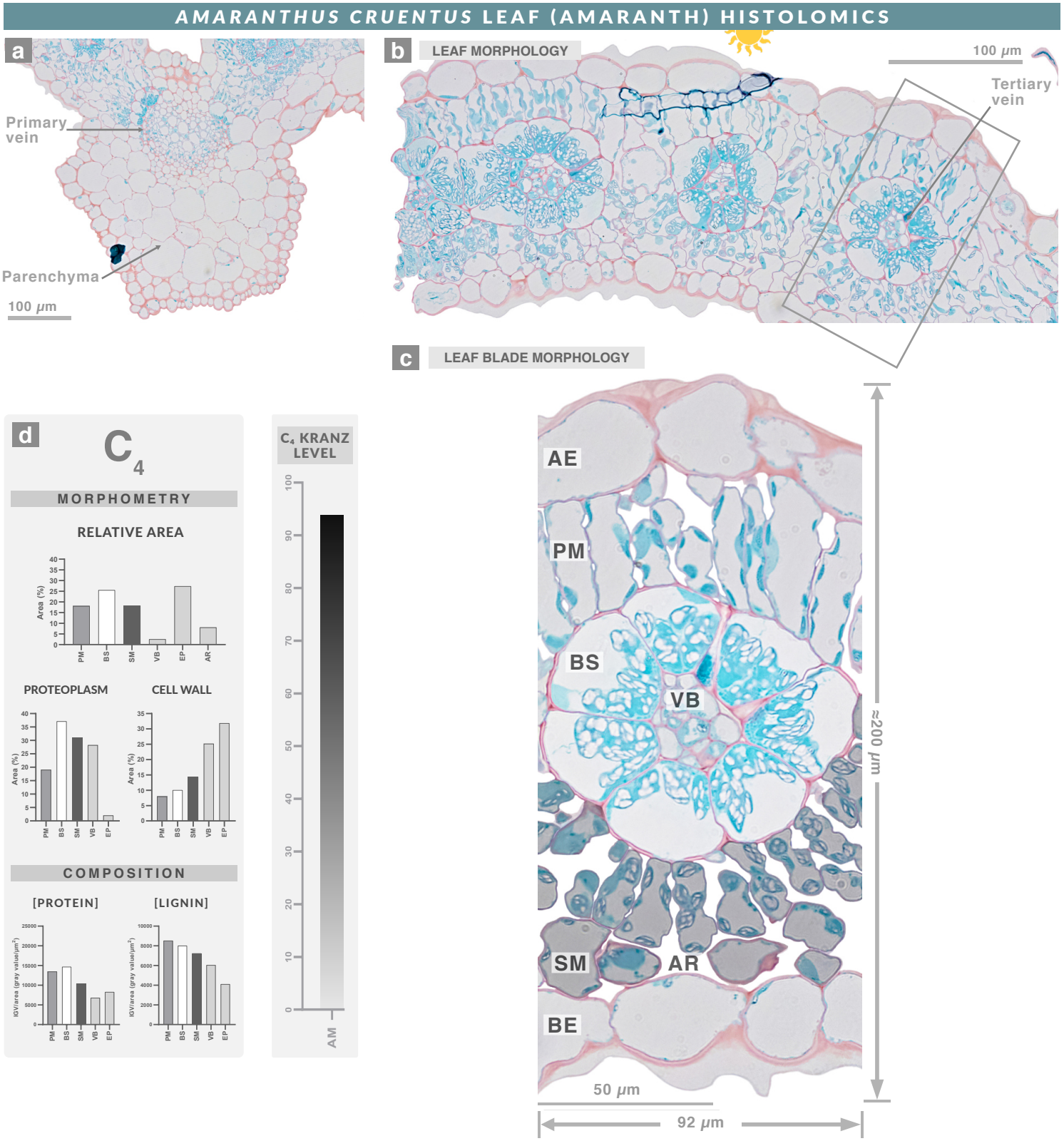

SUPPLEMENTARY FIGURE 21 **Histolome of *Amaranthus cruentus* leaf**

Cross section of a trichrome-stained *A. cruentus* leaf midrib (**a**) and leaf blade (**b**). **c** Magnification of the squared area in b. **d** Derived (morphometry and composition) and composite (C_4 Kranz level) features of the tissue (same scales for all plant species). The leaf of *A. cruentus* had a large BS tightly surrounded by a layer of differentiated PM and two layers off SM: wreath-shaped. Additional details are reviewed in Supplementary Figure 11.

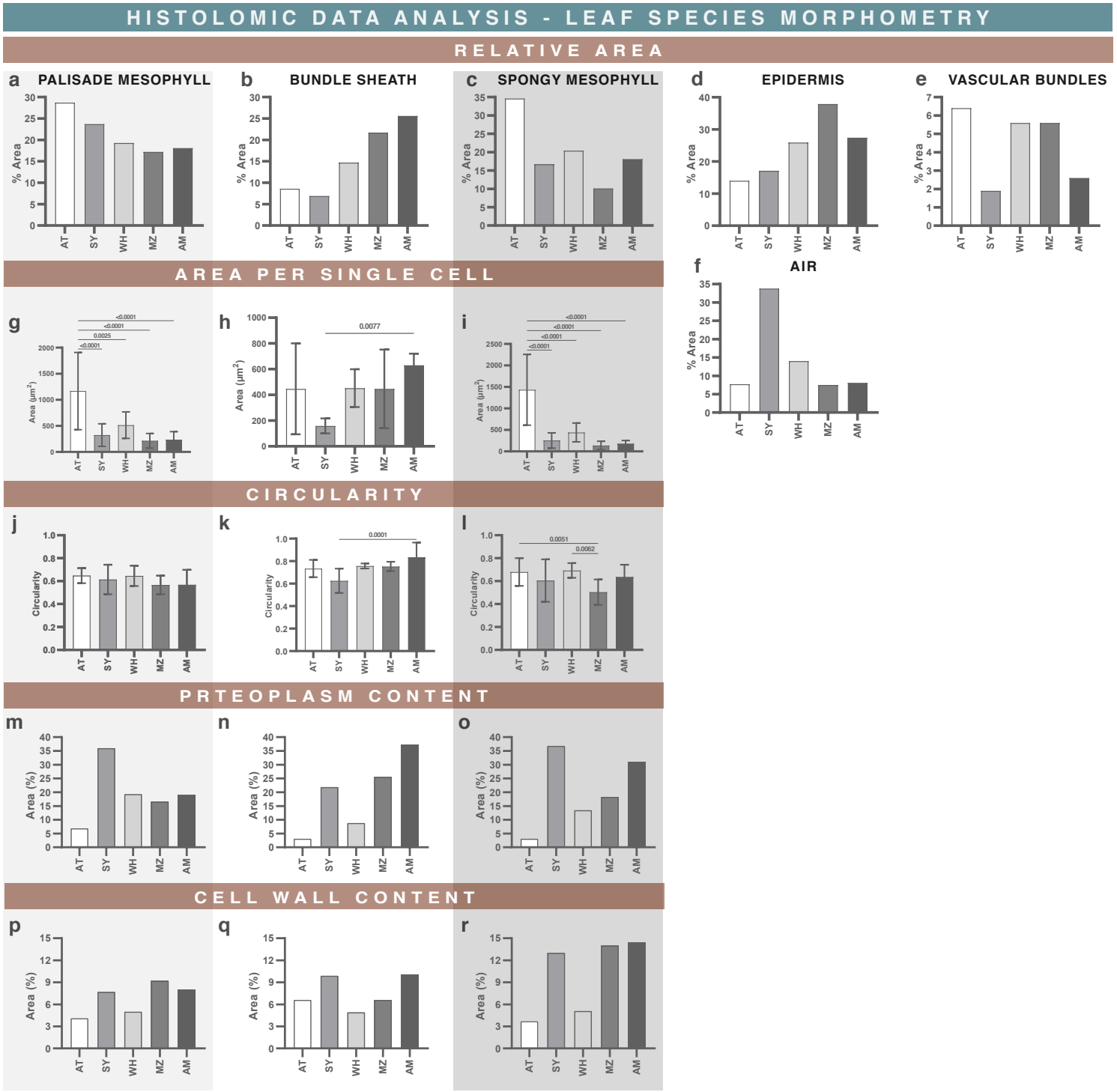

SUPPLEMENTARY FIGURE 22 **Histolomic morphometry analysis of different plant leaves**

Morphometric analysis of *A. thaliana* (AT), *G. max* (SY), *T. aestivum* (WH), *Z. mays* (MZ), and *A. cruentus* (AM) leaves. For measurements with replicates, a one-way ANOVA with Tukey's posttest was performed, values of $p<0.01$ are shown. Results are presented in ascending order of C_4 kranz level (AT, SY, WH, MZ, and AM), with the left being "most C_3" and the right being "most C_4". We put special emphasis on the mainly photosynthetic tissues: PM, SM and BS, which define the wreath shape and the global C_4 kranz anatomy. Some trends related to the increasingly C_4 kranz anatomy was observed: an increased BS (**b**) with more proteoplasm content (**n**), and a decreased PM (**a**) with less proteoplasm content (**m**). SM mesophyll did not show a clear trend, it tended to decrease (**c**), but its proteoplasm content tended to increase (**o**). BS cell wall increased thickness is another important feature of C_4 mesophyll anatomy; however, there was no trend (**p, q** and **r**). The epidermis showed an unexpected tendency to increase, interrupted only by the MZ (**d**), and vascular bundles showed no trend. Circularity failed to detect differences in shape; there were no significant differences between some PM and SM, although evident in the micrographs (**j, l**), but detected between BS of AM and SY, which indeed had similar shell shape (**k**). We expected and reduced the content of air spaces, since C_4 kranz plants are more efficient in fixing carbon, but there was none (**f**). Finally, AT had the greatest thickness, cell layers and cell sizes (**g, h, i**), but the lowest proteoplasm content (**m, n, o**).

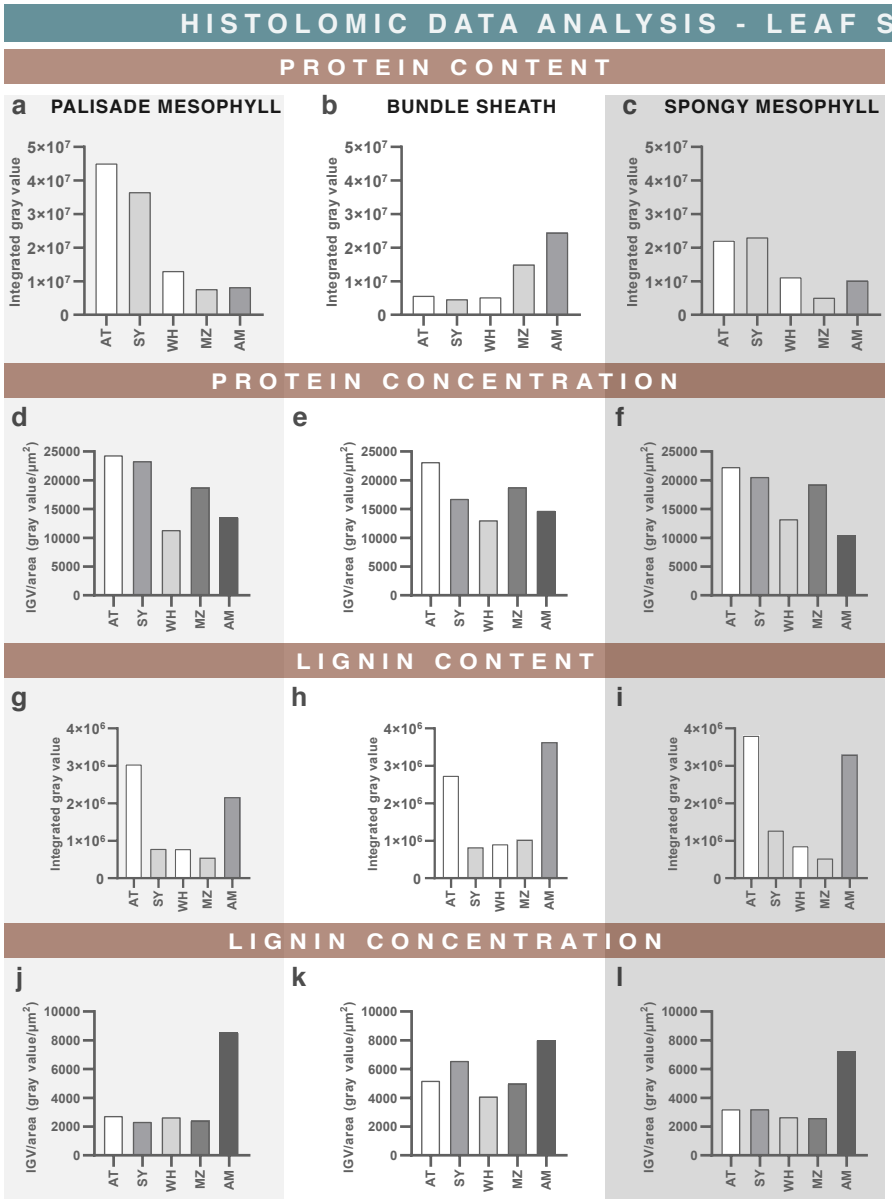

SUPPLEMENTARY FIGURE 23 **Histolomic compositional analysis of different plant leaves.**

Morphometric analysis of *A. thaliana* (AT), *G. max* (SY), *T. aestivum* (WH), *Z. mays* (MZ), and *A. cruentus* (AM) leaves. Results are presented in ascending order of C_4 Kranz level (AT, SY, WH, MZ, and AM), with the left being "most C_3" and the right being "most C_4". We put special emphasis on the mainly photosynthetic tissues: PM, SM and BS, which define the wreath shape and the global C_4 kranz anatomy. Some trends related to the increasing C_4 anatomy were observed: decreased protein content in PM and SM (**a, c**) and increased in BS (**b**), while protein concentration showed no trend (**d-f**). In contrast, lignin content and concentration showed no trend (**g - l**). However, AM tissues had the highest lignin concentration.

HISTOLOMIC DATA ANALYSIS - COMPOSITE FEATURES

a

#	Primary/ Derived Feature	Feature Score	Primary Features	AT Measurements	AT Absolute value	AT Weighted score	SY Measurements	SY Absolute value	SY Weighted score	WH Measurements	WH Absolute value	WH Weighted score	MZ Measurements	MZ Absolute value	MZ Weighted score	AM Measurements	AM Absolute value	AM Weighted score	Maximum absolute value
1	BS Size ratio	20	BS area (µm²) / M area (µm²)	8026 / 59276	0.12	5.4	1266 / 7395	0.15	6.6	4521 / 12201	0.27	12.2	3120 / 3921	0.44	20.0	4477 / 6336	0.41	18.7	0.44
2	BS organelle size ratio	20	BS PT area (µm²) / M PT area (µm²)	246 / 2843	0.08	2.9	277 / 2689	0.09	3.5	400 / 1993	0.17	6.2	798 / 675	0.54	20.0	1664 / 1587	0.51	18.9	0.54
3	Position of BS mitochondria	15	YES (1)/NO (0)	NO	0	0	NO	0	0	INTERMEDIATE	0.5	7.5	NO	0	0.0	YES	1	15	1
4	Position of BS chloroplast	15	YES (1)/NO (0)	NO	0	0	YES	1	15	NO	0	0	YES	1	15	YES	1	15	1
5	Wreath shape	15	YES (1)/NO (0)	NO	0	0	NO	0	0	YES	1	15	YES	1	15	YES	1	15	1
6	BS CW size ratio	5	BS CW area (µm²) / M CW area (µm²)	527 / 2289	0.19	2.4	125 / 731	0.15	1.9	222 / 616	0.26	3.4	206 / 430	0.32	4.1	453 / 709	0.39	5	0.39
7	BS CW lignin ratio	5	BS Lignin (IGV/area) / M Lignin (IGV/area)	5185 / 2981	1.74	3.7	6577 / 2772	2.37	5.0	4082 / 2648	1.54	3.2	4980 / 2504	1.99	4.2	8018 / 7885	1.02	2.1	2.37
8	BS air insulation	5	BS-M Contact perimeter (µm) / BS-AR Contact perimeter (µm)	493 / 77	0.86	5.0	62 / 140	0.31	1.8	153 / 246	0.38	2.2	175 / 114	0.61	3.5	228 / 61	0.79	4.6	0.86
	Total	100	C_4 Kranz level		3.0	19.4		4.1	33.7		4.1	49.7		5.9	81.8		6.1	94.3	

b

$$BS\ size\ ratio = \frac{Area_{BS}}{Area_{BS} + Area_{M}}$$

$$BS\ organelle\ size\ ratio = \frac{Area_{BS\ PT}}{Area_{BS\ PT} + Area_{M\ PT}}$$

$$BS\ CW\ size\ ratio = \frac{Area_{BS\ cw}}{Area_{BS\ cw} + Area_{M\ cw}}$$

$$BS\ CW\ lignin\ ratio = \frac{Lignin\ concentration_{BS}}{Lignin\ concentratio_{M}}$$

$$BS\ air\ insulation = \frac{Contact\ P_{BS-M}}{Contact\ P_{BS-M} + Contact\ P_{BS-AR}}$$

$$Weighted\ score = \frac{Absolute\ value}{Maximun\ absolute\ value} * \text{Trait score}$$

SUPPLEMENTARY FIGURE 24 **Calculation of the C_4 kranz anatomy level**

Calculation of the C_4 kranz level for *A. thaliana* (AT), *G. max* (SY), *T. aestivum* (WH), *Z. mays* (MZ), and *A. cruentus* (AM) leaves (**a**) and the formulas used (**b**). Bundle sheath (BS), Mesophyll (M), Cell Wall (CW), Proteoplasm (PT), Air Spaces (AR), Mitochondrion (MI), Chloroplast (CL) and Integrated Gray Value (IGV). Because individual comparisons of primary and derived features did not yield clear conclusions, they must be combined into a single value that allows for simple and quantitative comparisons. The primary features describe the individual characteristics of each tissue, such as: position of BS/mitochondria/chloroplast, which describes whether mitochondria/chloroplast are located centripetally (MI and CL) or centrifugally (CL) in BS, and wreath shape, which describes whether BS are large and tightly surrounded by a single layer of PM and SM (sometimes two PM layers). Derived features compare the primary features of two tissues, such as BS size ratio, which describes the size of BS tissue compared to M tissue. The same logic is used to compare organelle size, CW, lignin concentration, and air insulation. This set of morphometric and compositional features constitutes the C_4 kranz anatomy[1]. However, from our perspective, each of these features has a different degree of importance, so we have assigned them a score to calculate a weighted sum that reflects the overall "C_4 kranz level", a composite feature. It should be noted that the "C_4 Kranz level" is a histolomically based measurement and is used as an example of a histolomic application. It does not pretend to be an exhaustive description of C_4 photosynthesis, as it also implies the specific accumulation of some key enzymes such as Glycine decarboxylase complex in the mitochondrion; PEP carboxylase in the M cytosol, and RuBisCO and NADP-malic enzyme in the BS chloroplasts, and their contribution is not weighted here[1].

[1]Sage, R. F., Khoshravesh, R. & Sage, T. L. From proto-Kranz to C4 Kranz: building the bridge to C_4 photosynthesis. J. Exp. Bot. 65, 3341–3356 (2014)

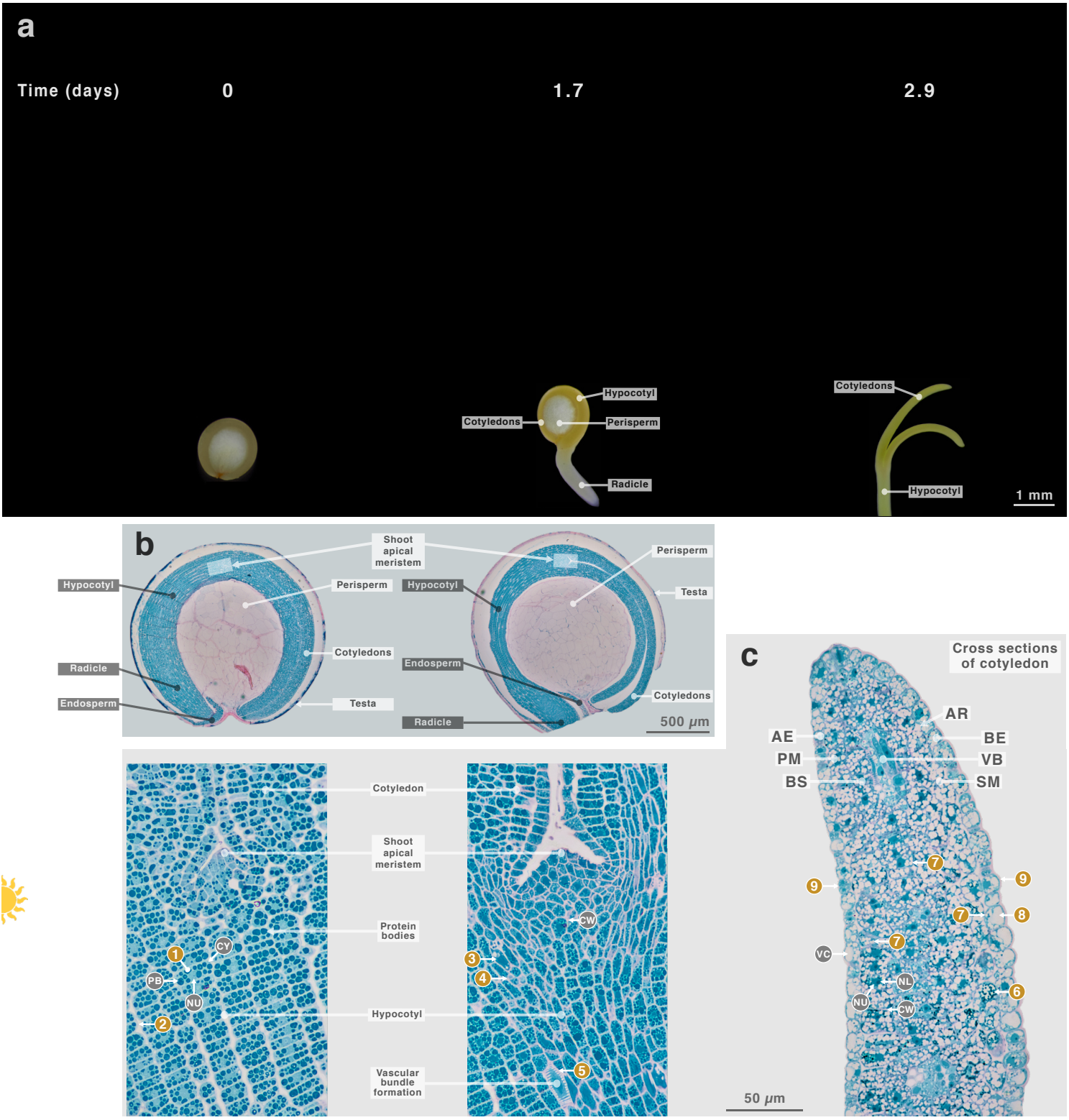

SUPPLEMENTARY FIGURE 25 **Histolomic visual analysis of *A. cruentus* seed germination**

a Polarization micrograph of amaranth seed at different germination stages. Days after sowing are indicated. **b** Light micrograph of a whole seed section (0 days), and in germination (1.7 days). **c** Magnification of the white boxed area in b, and a cross section of seedling cotyledon. The sections were stained with trichrome staining. Adaxial epidermis (AE), abaxial epidermis (BE), palisade mesophyll (PM), spongy mesophyll (SM), bundle sheath (BS), vascular bundles (VB), air spaces (AR). Cell wall (CW), vacuole (VC), chloroplast (CL), starch granule (ST), nucleus (NU), nucleolus (NL), cytosol (CY) and mitochondrion (MI). The resin-based microtechnique worked on amaranth seeds and seedlings. The embryo (cotyledons, hypocotyl and radicle) was stained turquoise, the testa magenta and the perisperm was not stained. The embryo was composed of fusiform cells whose proteoplasm contains mainly protein bodies, nucleus and cytosol (**1**). Their CW stained weakly, making them almost indistinguishable (**2**). After germination, the fusiform cells began to degrade their protein bodies (**3**), thickened their cell wall (**4**) and differentiated into conducting tissues such as tracheids (**5**). After three days, the cotyledon showed all the basic tissues of a leaf: AE, PM, BS, VB, SM, BE and some AR. Also, the protein bodies disappeared, but smaller and denser ones appeared (**6**), starch granules accumulated in almost all tissues (**7**), the epidermis formed vacuoles (**8**), and the BE formed a thicker outer wall than the AE outer wall.

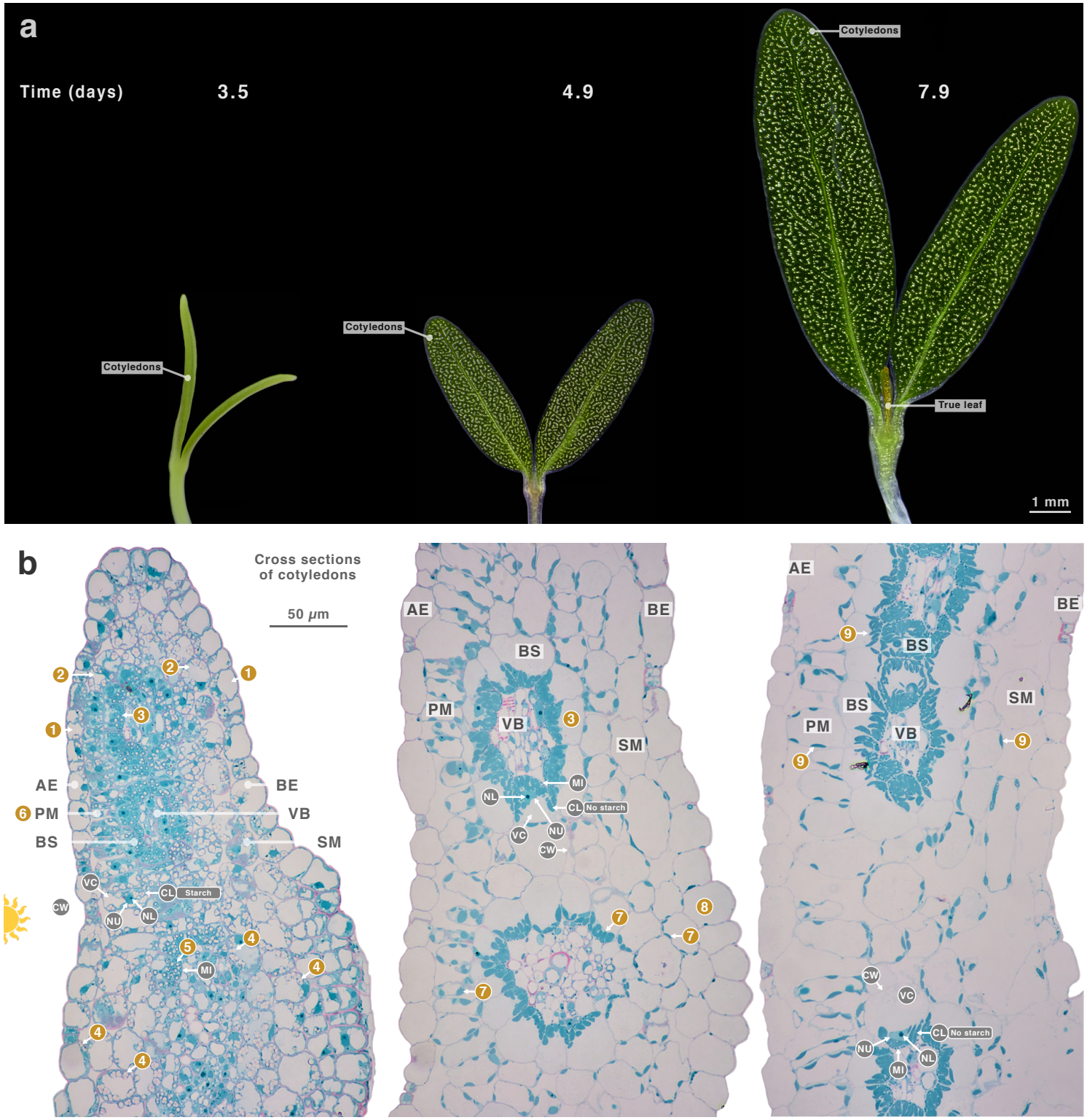

SUPPLEMENTARY FIGURE 26 **Histolomic visual analysis of *A. cruentus* cotyledon development**

a Polarization micrograph of amaranth cotyledons at different developmental stages. Days after sowing are indicated. **b** Light micrograph of a cross sections of the cotyledon in a. The sections were stained with trichrome staining. Adaxial epidermis (AE), abaxial epidermis (BE), palisade mesophyll (PM), spongy mesophyll (SM), bundle sheath (BS), vascular bundles (VB), air spaces (AR). Cell wall (CW), vacuole (VC), chloroplast (CL), starch granule (ST), nucleus (NU), nucleolus (NL), cytosol (CY) and mitochondrion (MI). After 3.5 days, all cells showed a clear development of organelles. Epidermal cells were the first to produce VC (**1**), followed by SM and PM (**2**), and finally BS (**3**). All cells except VB formed starch granules (**4**), the BS CL began to position themselves centripetally (**5**), and some PM began to acquire their characteristic rod-like shape (**6**). After 4.9 days, the cotyledon had a mature leaf-like morphology, all its ST disappeared (**7**) and the epidermal cells lost almost all their proteoplasm (**8**). Finally, after 7.9 days, the true leaf began to form, the cotyledon entered senescence and its chloroplasts took on a slender, curved shape (**9**).

TRICHROME STAINING OF A PARAFFIN SECTION

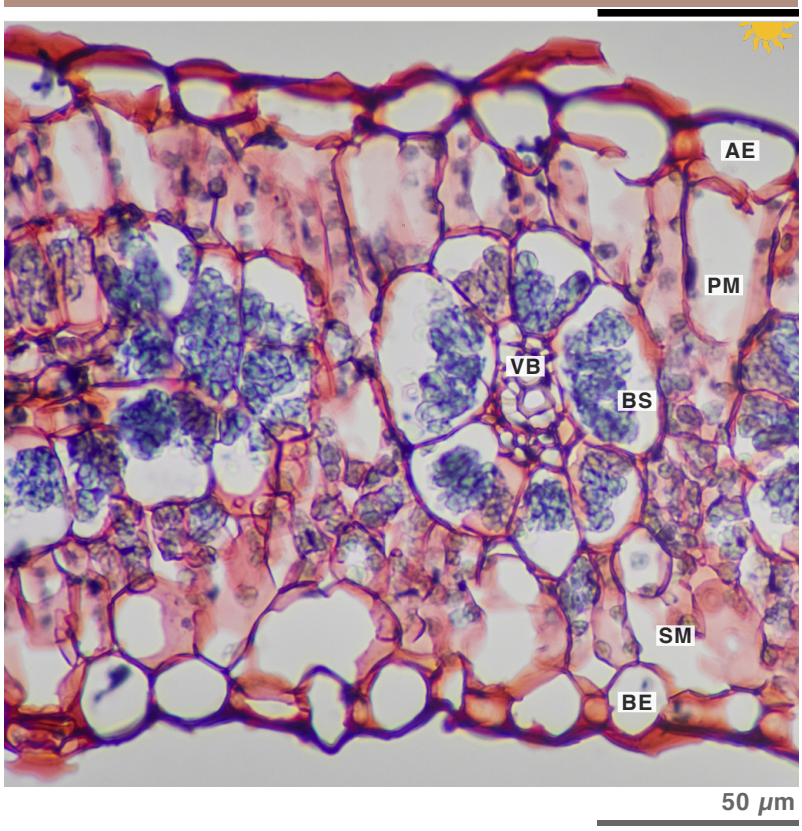

SUPPLEMENTARY FIGURE 27 **Trichrome staining also works on paraffin-embedded sections**

Light micrograph of a paraffin-embedded *A. cruentus* leaf section stained with trichrome staining. The section was not deparaffinized. Trichrome staining also worked on paraffin-embedded tissue. This section is 10 um thick, 20 times thicker than the resin sections. Therefore, the staining is more intense and the color of the starch granules masks the green of the chloroplasts. In addition, the cells of PM and SM contain important extensions of the cell wall, which is why they are mostly observed in a reddish color.